Article

# Structural basis of regulated m$^7$G tRNA modification by METTL1–WDR4

https://doi.org/10.1038/s41586-022-05566-4

Received: 22 May 2022

Accepted: 16 November 2022

Published online: 04 January 2023

Check for updates

Jiazhi Li[1,2,3,10], Longfei Wang[2,4,5,10], Quentin Hahn[1], Radosław P. Nowak[2,3], Thibault Viennet[2,3], Esteban A. Orellana[1,2], Shourya S. Roy Burman[2,3], Hong Yue[2,3], Moritz Hunkeler[2,3], Pietro Fontana[2,4], Hao Wu[2,4], Haribabu Arthanari[2,3], Eric S. Fischer[2,3] & Richard I. Gregory[1,2,6,7,8,9] ✉

Chemical modifications of RNA have key roles in many biological processes[1–3]. $N^7$-methylguanosine (m$^7$G) is required for integrity and stability of a large subset of tRNAs[4–7]. The methyltransferase 1–WD repeat-containing protein 4 (METTL1–WDR4) complex is the methyltransferase that modifies G46 in the variable loop of certain tRNAs, and its dysregulation drives tumorigenesis in numerous cancer types[8–14]. Mutations in *WDR4* cause human developmental phenotypes including microcephaly[15–17]. How METTL1–WDR4 modifies tRNA substrates and is regulated remains elusive[18]. Here we show, through structural, biochemical and cellular studies of human METTL1–WDR4, that WDR4 serves as a scaffold for METTL1 and the tRNA T-arm. Upon tRNA binding, the αC region of METTL1 transforms into a helix, which together with the α6 helix secures both ends of the tRNA variable loop. Unexpectedly, we find that the predicted disordered N-terminal region of METTL1 is part of the catalytic pocket and essential for methyltransferase activity. Furthermore, we reveal that S27 phosphorylation in the METTL1 N-terminal region inhibits methyltransferase activity by locally disrupting the catalytic centre. Our results provide a molecular understanding of tRNA substrate recognition and phosphorylation-mediated regulation of METTL1–WDR4, and reveal the presumed disordered N-terminal region of METTL1 as a nexus of methyltransferase activity.

Recent 'epitranscriptome' studies have revealed critical roles of RNA modifications in various molecular, cellular and developmental processes[1,2]. Several childhood developmental disorders are caused by mutations in genes encoding RNA-modifying enzymes, and dysregulation of certain RNA modifications is oncogenic[3,19,20]. tRNAs are the most highly modified class of RNAs that influences tRNA maturation, stability and function[4,21,22]. Of these, m$^7$G at position G46 (m$^7$G46) in the variable loop is a prevalent modification in a large subset of tRNAs. m$^7$G46 interacts with C13–G22 in the D-loop to stabilize tRNA tertiary structure[5]. Impaired m$^7$G46 is associated with rapid tRNA decay and altered expression[6,7]. m$^7$G46 is catalysed by METTL1 and its essential cofactor WDR4 (refs. [8,9]). The METTL1–WDR4 complex is required for normal mRNA translation and mouse embryonic stem cell proliferation and differentiation[23]. Mutations in *WDR4* are associated with developmental defects including primordial dwarfism, microcephaly and Galloway–Mowat syndrome[15–17]. Dysregulated METTL1–WDR4 drives tumorigenesis and this oncogenic function is linked to numerous different cancer types[10–14]. However, the lack of structural and mechanistic information on human METTL1–WDR4 remains a major obstacle to elucidating the m$^7$G46 modification process and development of methyltransferase (MTase) inhibitors as possible new anticancer drugs.

m$^7$G46 modification occurs in a large subset of tRNAs that contain the 'RAGGU' motif within the variable loop[10,11,23]. In vitro MTase assays showed the importance of the D-arm and T-arm for m$^7$G modification by the yeast Trm8–Trm82 complex (which are orthologues of METTL1 and WDR4, respectively)[24]. A model for tRNA recognition was previously generated by computationally docking a tRNA structure into a structure of Trm8–Trm82 (ref. [9]). The model implicated tRNA interaction with the positively charged surface of Trm8 without contact with Trm82 and is based on only a partial structure of the yeast complex that lacks regions required for m$^7$G catalysis. It therefore remains unknown how the m$^7$G MTase complex specifically engages and modifies tRNA substrates.

Phosphorylation of METTL1 (S27) by protein kinase B (also known as AKT) can inactivate MTase activity by an unknown mechanism[18]. Notably, S27 is located within the N terminus of METTL1, for which no structural information is available and is predicted to be largely disordered[9]. Nevertheless, the flexible METTL1 N terminus is conserved, implying essential functions.

Here we report structures of the human METTL1–WDR4 heterodimer, and in complex with tRNA substrates, tRNA$^{Val}$TAC and tRNA$^{Phe}$GAA. The different tRNAs show a similar binding mode to METTL1–WDR4, in which the structural rearrangement of both the MTase complex and the tRNA are visualized. Combined with functional assays, we uncover

[1]Stem Cell Program, Division of Hematology/Oncology, Boston Children's Hospital, Boston, MA, USA. [2]Department of Biological Chemistry and Molecular Pharmacology, Harvard Medical School, Boston, MA, USA. [3]Department of Cancer Biology, Dana-Farber Cancer Institute, Boston, MA, USA. [4]Program in Cellular and Molecular Medicine, Boston Children's Hospital, Boston, MA, USA. [5]School of Pharmaceutical Sciences, Wuhan University, Wuhan, China. [6]Division of Hematology/Oncology, Boston Children's Hospital, Boston, MA, USA. [7]Department of Pediatrics, Harvard Medical School, Boston, MA, USA. [8]Harvard Stem Cell Institute, Cambridge, MA, USA. [9]Harvard Initiative for RNA Medicine, Boston, MA, USA. [10]These authors contributed equally: Jiazhi Li, Longfei Wang. ✉e-mail: rgregory@enders.tch.harvard.edu

the molecular mechanism for m$^7$G46 modification by METTL1–WDR4. We identify an essential role for the METTL1 N terminus (residues 1–33), which, although anticipated to be unstructured, has a key role in the formation of the MTase catalytic pocket. We furthermore uncover how S27 phosphorylation in the N-terminal domain of METTL1 inhibits MTase activity via a steric interference mechanism in the active site. Our findings uncover the molecular mechanism of tRNA substrate recognition by METTL1–WDR4, highlight the unanticipated role of the N-terminal region of METTL1 in tRNA modification and explain the phospho-mediated regulation of MTase activity.

## Structures of METTL1–WDR4–tRNA

To visualize how human METTL1–WDR4 binds to tRNA, we pursued cryo-electron microscopy (cryo-EM) studies of the METTL1–WDR4–tRNA$^{Phe}$ and METTL1–WDR4–tRNA$^{Val}$ complexes (Extended Data Fig. 1a–c). Monodisperse ternary complex samples were obtained using size-exclusion chromatography and examined using native polyacrylamide gel electrophoresis (PAGE) before cryo-EM screening and data collection (Extended Data Fig. 1d,e). Reconstructions of the METTL1–WDR4–tRNA$^{Phe}$ complex with *S*-adenosylhomocysteine (SAH) were refined to 3.3 Å (Fig. 1a and Extended Data Fig. 2a) and the METTL1–WDR4–tRNA$^{Val}$ complex to 3.6 Å (Extended Data Fig. 2b). Although both maps are anisotropic and to some extent challenging to accurately interpret in regions such as the distal part of WDR4 and tRNA (Extended Data Fig. 2c–h), model building in these regions was guided by a crystal structure obtained for the METTL1–WDR4 binary complex (Fig. 1b–d), AlphaFold2 predictions and published tRNA structures[25,26]. In both ternary complexes, the overall structures resemble a sail-boat-like arrangement with METTL1 and WDR4 as the stern and bow, respectively, and the tRNA as the sail that sits on top of METTL1–WDR4 and tilts sideways (Fig. 1b,c and Extended Data Fig. 3a–d).

METTL1, like other members of the class I MTase family, shared the highly conserved Rossmann-like fold, comprising a seven-strand β-sheet flanked by six α-helices (Fig. 1b and Extended Data Fig. 4). WDR4 adopts a β-propeller structure with seven blades (B1–B7) (Extended Data Fig. 5a,b). The B2–B5 region of WDR4, which is in proximity to METTL1, is highly conserved (Extended Data Fig. 5c).

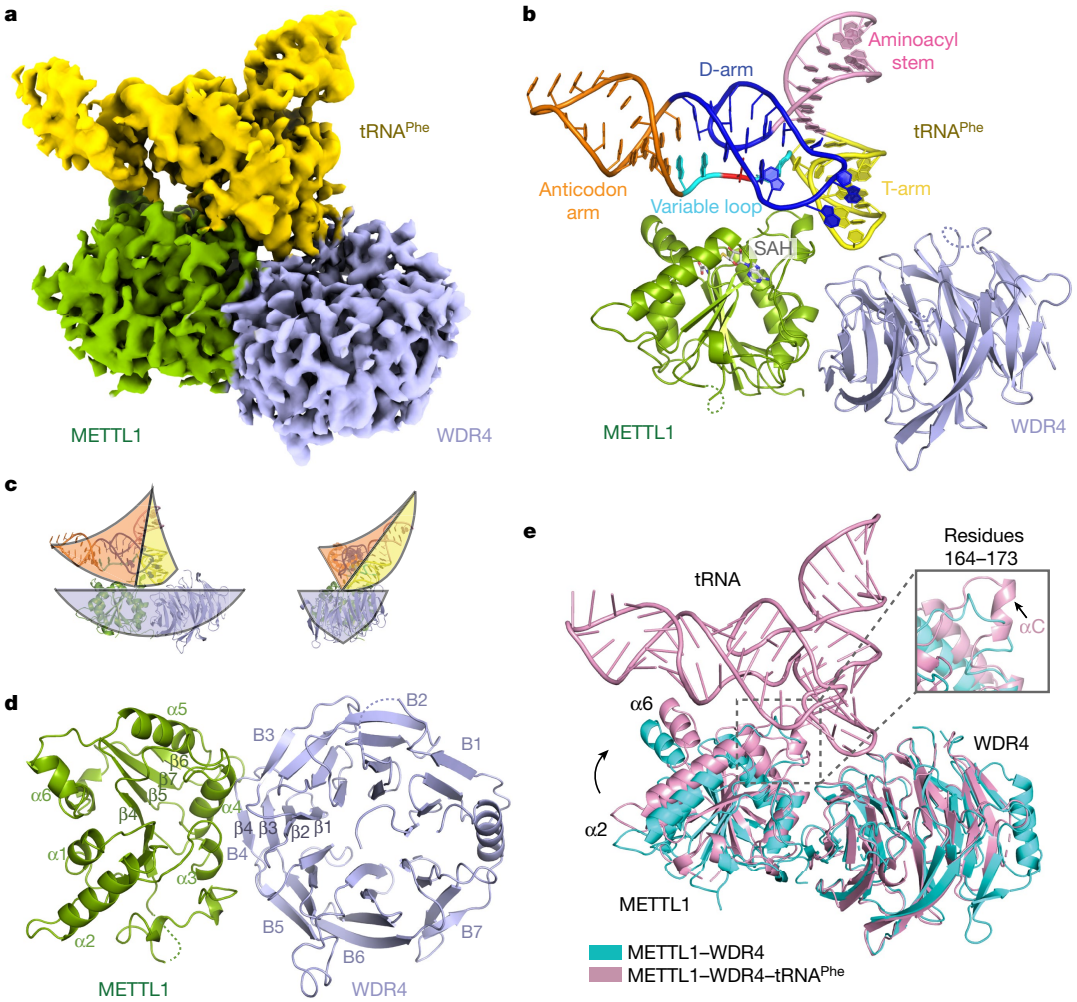


**Fig. 1 | METTL1–WDR4 provides a platform for specific tRNA loading.** **a**,**b**, Cryo-EM density map of the METTL1–WDR4–tRNA$^{Phe}$ complex (**a**) and the corresponding atomic model (**b**). The sharpened map is shown. METTL1 is in coloured in green, WDR4 in light purple and tRNA$^{Phe}$ in yellow. tRNA domains are coloured according to Extended Data Fig. 1a. G46 is highlighted in red. The missing regions are shown as dashed lines. **c**, Sail-boat model of the METTL1–WDR4–tRNA$^{Phe}$ ternary complex in side view (left) and front view (right). **d**, X-ray crystal structure of the full-length METTL1–WDR4 binary complex. METTL1 (green) and WDR4 (light purple) are shown in cartoon representation. Secondary structural elements of α-helix (α) and β-sheet (β) are numbered. The missing regions are shown as dashed lines. **e**, Structural comparison between the METTL1–WDR4–tRNA$^{Phe}$ complex (pink) and the METTL1–WDR4 binary complex (cyan). The two structures are superimposed on WDR4 proteins. Magnified view of METTL1 (residues 164–173) shows the αC helix that is formed upon tRNA binding.

## tRNA loading by METTL1–WDR4

To investigate whether tRNA binding causes structural rearrangements of METTL1–WDR4, we determined the crystal structure of the human METTL1–WDR4 binary complex to a resolution of 3.1 Å (Fig. 1d). In the crystal structure, the entire β-propeller of WDR4 and the following α-helix (residues 319–348) were modelled, but residues 26–33 from the N-terminal of METTL1 were not visible. Although the overall assembly of METTL1 and WDR4 was similar without tRNA, a superposition on WDR4 showed substantial changes in METTL1 upon tRNA binding (Fig. 1e and Extended Data Fig. 6a). Four helices of METTL1 (α1, α2, α5 and α6) are shifted towards the tRNA. A loop (residues 164–173) connecting α1 and the core of the Rossmann fold of METTL1 forms a $3_{10}$ helix (hereafter referred to as the αC helix), which is inserted into the groove of the tRNA elbow region. Despite being highly conserved among eukaryotes (Extended Data Fig. 4), the residues 164–173 represent either a loop or are disordered in all known METTL1 structures (Protein Data Bank (PDB) 3CKK, 7PL1, 2VDU and 2VDV). When superimposing the METTL1 structures in its tRNA-free and tRNA-bound states, the αC loop is the only region that undergoes structural rearrangement, suggesting that the αC helix of METTL1 facilitates tRNA recognition (Extended Data Fig. 6b and discussed later).

About 28% of the particles from the METTL1–WDR4–$tRNA^{Phe}$ dataset represent the binary complex and were used to reconstruct a cryo-EM map with a resolution of 3.5 Å (Extended Data Fig. 6c). Although the overall structure of the cryo-EM binary complex is similar to the crystal structure (Extended Data Fig. 6d), local resolution of the αC region was low and we were unable to model the αC region confidently (Extended Data Fig. 6e,f).

The non-catalytic subunit WDR4 is required for MTase activity[8]. To explore the mechanistic basis for this requirement, we further analysed the interface between METTL1 and WDR4 in the binary structure, and found that B4 of WDR4 contributes most interactions between the two proteins (Extended Data Fig. 7a). Salt bridges (between METTL1 K143 and WDR4 D166, and between METTL1 D261 and WDR4 H178), and hydrogen bonds (METTL1 Y37 and WDR4 E167, METTL1 N147 and WDR4 K168, and METTL1 K40 with the backbone of WDR4 L185) form the interface between METTL1 and WDR4. METTL1 K143, WDR4 D166 and WDR4 E167 are conserved among different species (Extended Data Figs. 4 and 5b). Single alanine substitutions of some of these conserved residues abolished MTase activity (Extended Data Fig. 7b). In *Mettl1*-knockout (KO) or *Wdr4*-KO cell lines (R1/E mouse embryonic stem cells), the METTL1 K143A, WDR4 D166A and WDR4 E167A variants could not rescue $m^7G$ tRNA modification (Extended Data Fig. 7c,d). Thus, the interactions between METTL1 and B4 of WDR4 are necessary for MTase activity.

## WDR4 acts as a scaffold for tRNA binding

We found that B4 of WDR4 not only mediates the interaction with METTL1 but is also, together with B3, involved in tRNA binding (Fig. 2a,b). Positively charged residues are located on the top of B3 and B4, and are prone to form salt bridges with the phosphates of the T-arm of tRNA. Alanine substitutions of these residues showed varying effects with little effect on MTase activity of R103A, R104A and K122A, reduced activity with K83A, and no activity was observed for R165A or the R103;R104A double mutant (Fig. 2c).

Mutation of R170, located in B4 of WDR4, is a mutation linked to primordial dwarfism accompanied by distinct facial dysmorphism, brain malformation and severe encephalopathy with seizures[15,17]. The presumed corresponding residue (K223) in yeast Trm82 (WDR4) forms a salt bridge with E204 of Trm8 (METTL1) (Extended Data Fig. 7e). On the basis of the Trm8–Trm82 structure, it was proposed that R170 variants disrupt the interaction of WDR4 with METTL1 (ref. [15]). We find that, in human, the R170 of WDR4 probably does not interact with METTL1 but rather mediates intramolecular WDR4 interactions (Fig. 2b and Extended Data Fig. 7e,f). These comparisons were performed using the crystal structure of the METTL1–WDR4 binary complex as the relevant region is better resolved. The side chain of R170 forms hydrogen bonds with the main chain of G143 and P177, which are located in B3 and B4, respectively. Right alongside R170, the H144 of WDR4 B3 interacts with D164 and T162 of B4. On the basis of The Cancer Genome Atlas data, the H144P mutation occurs in lung cancer, yet the mechanism and effect on the activity of the MTase complex are unknown. The in vitro MTase assay showed that R170Q and H144P variants totally abolished the MTase activity of METTL1, and the R170L variant decreased activity by one-third (Fig. 2d). Therefore, these patient-derived mutation sites are involved in B3–B4 stabilization and are crucial for MTase activity.

To further verify the role of WDR4, we also tested the effects of individual amino acid substitutions of WDR4 in cells (Fig. 2e and Extended Data Fig. 7g). The level of $m^7G$ was almost undetectable in rescue experiments using R170L, R170Q and H144P WDR4 variants in *Wdr4*-KO cells. Similarly, charge reversal (mutated to E) of R165 and R103;R104 was also incapable of rescuing the levels of $m^7G$ when introduced into WDR4-deficient cells. Together, we identify that WDR4 acts as a scaffold to interact with METTL1 and support tRNA binding. Importantly, mutations that impair the rigidity of the scaffold decrease MTase activity.

## tRNA bending by METTL1–WDR4

The tRNA G46 is buried in the variable loop (Fig. 1b and Extended Data Fig. 1a) and needs to be flipped into the catalytic site for modification by METTL1, which could be induced by tRNA bending[9,27]. 3D variability analysis performed with cryoSPARC[28] suggested that the $tRNA^{Phe}$ underwent bending (Supplementary Video 1), and we therefore clustered particles based on the principal components in the 3D variability analysis and selected two distinct clusters from METTL1–WDR4–$tRNA^{Phe}$ for reconstructions (Extended Data Fig. 2a). Superposition of models that were rigid body fit to the maps of the two states (named state A, pre-bending; and state B, bending) showed that, although the position of most of the $tRNA^{Phe}$ remained unchanged relative to the MTase, the anticodon arm was bent towards METTL1 and accompanied with local unwinding of the variable loop (Fig. 2f and Extended Data Fig. 2h). METTL1 is closer to the tRNA in state B than in state A. As a result, the variable loop is positioned closer to the catalytic pocket of METTL1 and is partially unwound, which probably facilitates base flipping of tRNA G46.

## METTL1 recognizes tRNA via two helices

Owing to the induced fit, side-chain densities for the METTL1 αC and α6 helices are absent from the experimental density but the atoms in the main chain can be traced with high confidence (Extended Data Fig. 2g). These two helices contain multiple conserved and positively charged residues (Fig. 2g,h and Extended Data Fig. 4). METTL1 H165, K167, R168 and K170 of αC are close to the T-arm and variable loop junction (T–V joint), and the K243 and R246 of α6 helix are close to the anticodon arm and variable loop junction (A–V joint). MTase activity was decreased by alanine-substituted mutations of H165, K170 and K167 in αC (Fig. 2i). Single mutation of METTL1 K243 and R246 in α6 slightly decreased MTase activity, but the double mutation decreased the activity by half. In vivo, the METTL1 αC and α6 variants (K243A;R246A, H165, K167A and K170A) were unable to rescue the level of $m^7G$ (Fig. 2j and Extended Data Fig. 7h). These results support a model in which METTL1 binds to the tRNA variable loop through two helices but requires WDR4 as a 'scaffold' (Fig. 2k). B4 of WDR4 serves as an important bridge between WDR4 and METTL1.

## Role of the N terminus in METTL1 activity

The N-terminal region (residues 1–33) of METTL1 is predicted to be disordered, consistent with the lack of electron density in crystal structures

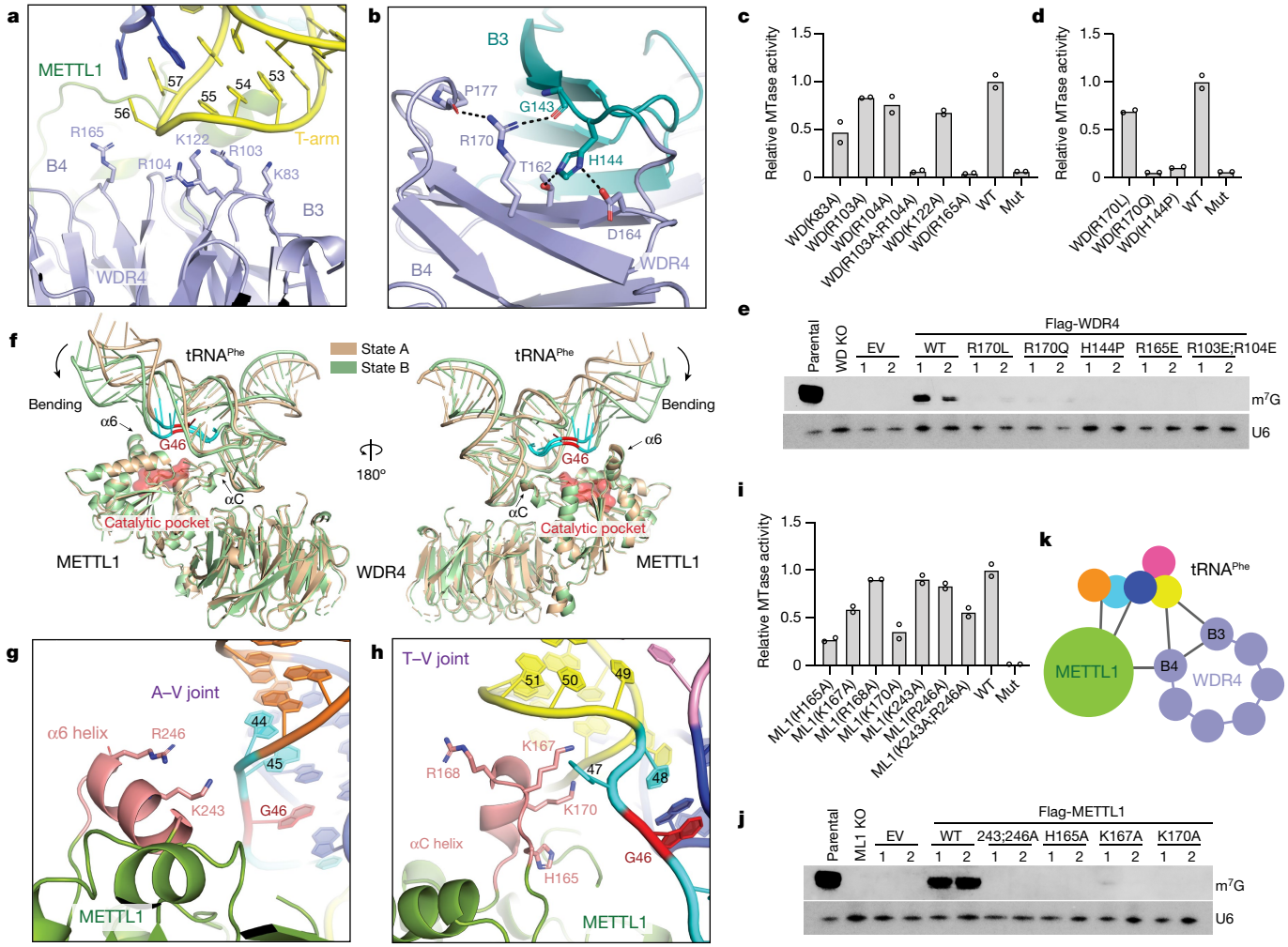


**Fig. 2 | tRNA recognition by METTL1 and WDR4. a**, WDR4 binds to the T-arm of $tRNA^{Phe}$. Positively charged residues on B3 and B4 are modelled based on the crystal structure. Nucleotides 53–57 of the tRNA are indicated. **b**, Interactions between WDR4 B3 (dark teal) and B4 (light purple) in the crystal structure of METTL1–WDR4. The interactions of disease-related sites, R170 and H144, are highlighted by dashed lines. **c**,**d**, Relative MTase activity of the indicated mutations in **a** (**c**) and **b** (**d**). Two technical replicates were performed. Mut, catalytic dead mutant (L160A;D163A); WT, wild type. **e**, In vivo rescue experiment with WDR4 carrying the patient-derived mutations and tRNA-binding site mutations. $n = 2$, biologically independent samples. For protein expression, see Extended Data Fig. 7e. For gel source data, see Supplementary Fig. 1. EV, empty vector; WD KO, *Wdr4* knockout. **f**, Superposition of different states of the METTL1–WDR4–$tRNA^{Phe}$ complex in two views. The two structures are superimposed on METTL1 proteins. G46 and the catalytic pocket are highlighted in red, and the tRNA variable loop in cyan. **g**,**h**, Helices αC and α6 of METTL1 recognize tRNA. Magnified view of the αC helix interacts with the T–V joint (**h**) and the α6 helix with the A–V joint (**g**). The variable loop is coloured in cyan, and the αC and α6 helices in salmon. The T–V and A–V joints are the joint regions of variable loop with the T-arm and anticodon arm, respectively. Nucleotides 44–51 of the tRNA are indicated. Positively charged residues on αC and α6 helices are modelled based on the crystal structure. **i**, Relative MTase activity of METTL1 (ML1)–WDR4 complexes expressed with indicated mutations. Two technical replicates were performed. **j**, In vivo rescue experiment with METTL1 variants relative to **i**. $n = 2$, biologically independent samples. For protein expression, see Extended Data Fig. 7f. For gel source data, see Supplementary Fig. 1. **k**, Scaffold model of METTL1 (green), $tRNA^{Phe}$ (colour coded relative to Fig. 1b) and WDR4 (light purple; B3 and B4 are labelled).

of the human METTL1 (PDB 3CKK and 7OGJ), the yeast orthologue (PDB 7VDC and 2VDU) and our crystal structure of the METTL1–WDR4 binary complex (Extended Data Fig. 8a). However, the high degree of amino acid sequence conservation (residues 16–50) and the presence of a regulatory phosphorylation site (S27) that inhibits METTL1 activity[18] point towards an important role of the N terminus (Extended Data Fig. 4). We therefore analysed the AlphaFold[25] predicted structure of a METTL1–WDR4 dimer (Fig. 3a and Extended Data Fig. 8b), which, consistent with our structures, has residues 34–54 attached to the surface of METTL1 and extending towards the catalytic pocket (Figs. 1b,d and 3a,b). Residues 16–33 (AlphaFold) thread through the catalytic pocket of METTL1, with residues 28–32 turning and entering the catalytic pocket where H26 and S27 are buried. In our ternary cryo-EM structures, the weak density for residues 26–33 can be traced and agrees well with the predictions from AlphaFold (Fig. 3a,b and Extended Data Fig. 2g), indicating that the 26–27 segment contributes to the catalytic pocket. Residues 21–25 were predicted to exit and contact one end of the METTL1 α2 helix, which might act as an anchor for residues 16–20 (Extended Data Fig. 8c). When superposing the predicted METTL1 structure onto the ternary complex structure, the 16–20 segment is positioned between the α2 helix and tRNA, which potentially interacts with tRNA (Extended Data Fig. 8d).

To investigate whether the N terminus binds to the METTL1 core, we utilized nuclear magnetic resonance (NMR). We expressed the isotope-labelled 1–75 segment of METTL1 and confirmed that it is largely disordered, except for the 45–55 segment that exhibits secondary structure (Extended Data Fig. 8e). We then used NMR titration experiments to map the interaction of the METTL1 core onto its

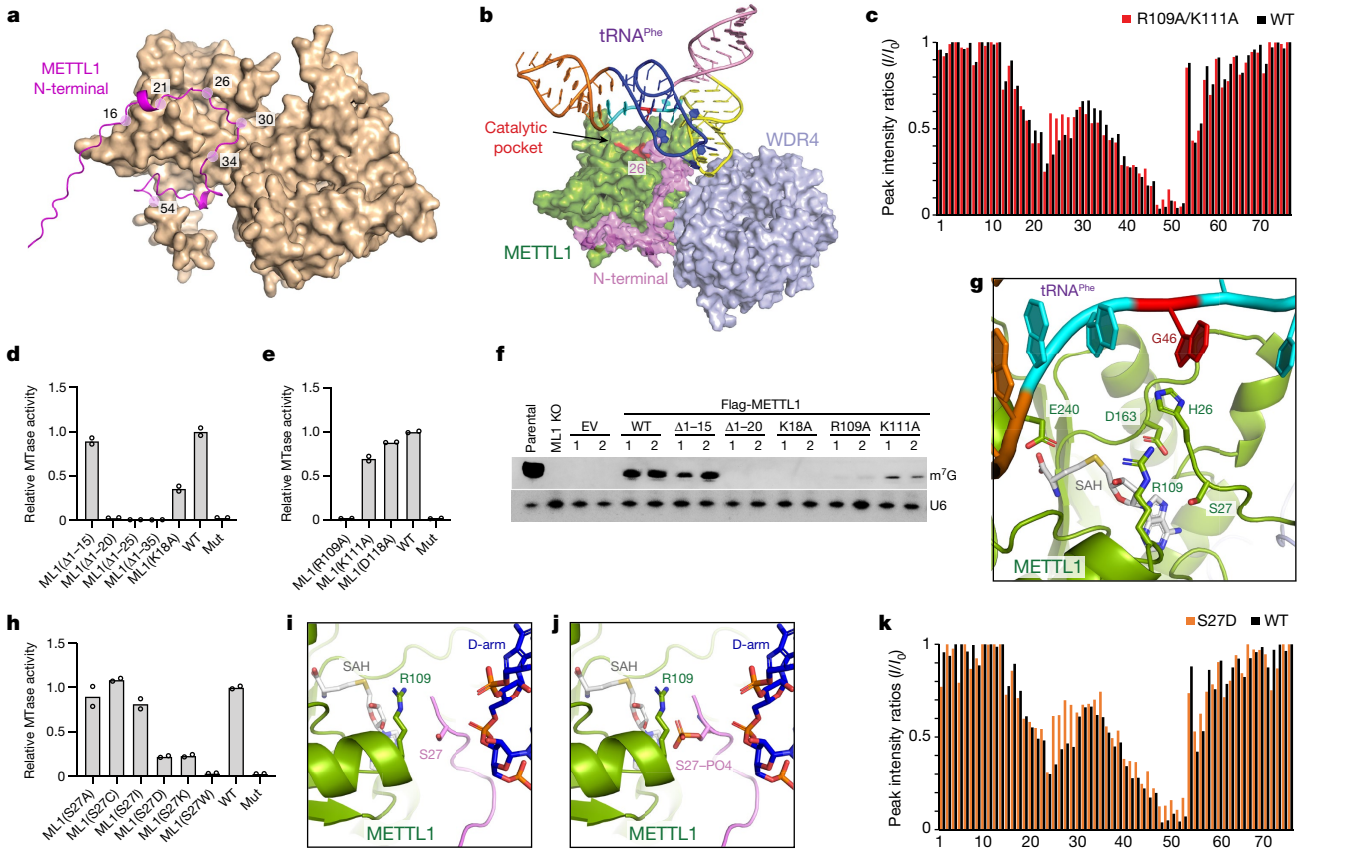


**Fig. 3 | The essential roles of the METTL1 N terminus. a**, AlphaFold prediction of METTL1–WDR4. The METTL1 N-terminal (residues 1–54) is in cartoon representation (magenta) and annotated residues are highlighted. Residues 366–412 of WDR4 are hidden for better view. The IDDT is shown in Extended Data Fig. 8b. **b**, The METTL1 N terminus (magenta) inserts into the catalytic pocket (red) in the METTL1–WDR4–tRNA$^{Phe}$ cryo-EM structure. Proteins are shown in surface representation. The location of residue 26 is highlighted. **c**, NMR peak intensity ratios plotted against the METTL11–75 sequence. Ratios are calculated as $I/I_0$ corresponding to the $^{15}$N–$^{1}$H-HSQC spectra of METTL11–75 in the presence of 10 molar equivalent of full-length WT METTL1 (black) or R109A/K111A METTL1 (red) divided by those of METTL11–75. **d**,**e**, Relative MTase activity of METTL1–WDR4 complexes expressed with indicated truncations or mutations. Two technical replicates were performed. **f**, In vivo rescue experiment with METTL1 variants. $n = 2$, biologically independent samples. For protein expression, see Extended Data Fig. 8g. For gel source data, see Supplementary Fig. 2. **g**, The catalytic pocket of METTL1 in METTL1–WDR4–tRNA$^{Phe}$. Relative residues are shown in stick representations. G46 is highlighted in red. **h**, Relative MTase activity of METTL1–WDR4 complexes expressed with the indicated METTL1 mutants. Two technical replicates were performed. **i**,**j**, Steric hindrance model of S27 phosphorylation. Side chains are modelled based on AlphaFold prediction. The side chain of S27 points to R109 (**i**). Substitution of S27 for its phosphorylated analogue leads to a steric clash with R109 (**j**). **k**, NMR peak intensity ratios plotted against the METTL11–75 sequence. Ratios are calculated as $I/I_0$ corresponding to the $^{15}$N–$^{1}$H-HSQC spectra of WT METTL11–75 (black) or S27D METTL11–75 (orange) in the presence of 10 molar equivalent of full-length WT METTL1 divided by those of the corresponding METTL11–75.

N terminus. Notably, we observed two interacting segments: residues 35–55 that interact with higher affinity (this corresponds to the segment seen in our binary complex structure and the element possessing secondary structure) and residues 18–27 that interact with an apparent lower affinity (Fig. 3c, wild type, black). These results confirm that residues 18–27 associate with the METTL1 core.

To probe the functional importance of the N terminus, we performed truncation and mutagenesis studies on the N terminus and the α2 helix of METTL1 in vitro. Truncation studies show that deletion of residues 1–15 of METTL1 has little effect on MTase activity, but deletion of residues 1–20 or more leads to an inactive enzyme (Fig. 3d). The single alanine substitution of K18 of METTL1 substantially decreased MTase activity. In the time-resolved Förster resonance energy transfer (TR-FRET) competitive binding assay, the binding affinity of METTL1(Δ1–20 amino acids)–WDR4 and METTL1(Δ1–36 amino acids)–WDR4 truncations to tRNA was slightly lower than full-length METTL1–WDR4 (Extended Data Fig. 8f). These results are consistent with our proposed role of residues 16–20 in MTase activity and possible contact with the anticodon branch of tRNA. Single alanine substitution of K111 and D118 (α2) showed moderate effect on the methylation activity of METTL1, but R109A (α2) totally abolished the activity (Fig. 3e). Furthermore, NMR experiments showed that the R109A;K111A mutation in the α2 helix decreased its association with residues 24–27 in the N-terminal region of METTL1 (Fig. 3c, R109A/K111A, red). We also validated these results with in vivo experiments (Fig. 3f and Extended Data Fig. 8g). The METTL1 R109A and K18A (N terminus) mutants were unable rescue the level of m$^7$G in *Mettl1*-KO mouse embryonic stem cell lines, whereas K111A could partially rescue m$^7$G tRNA modification. METTL1(Δ1–15 amino acids) completely restored m$^7$G tRNA modification, whereas METTL1(Δ1–20 amino acids) did not rescue m$^7$G tRNA modification. Therefore, residues 16–27, as a highly conserved part of the METTL1 catalytic pocket, are essential for METTL1 activity.

## Phosphorylation regulation of METTL1

Human METTL1 is inactivated by AKT-mediated S27 phosphorylation[18]. This phosphorylation site is located at the bottom of the U-shaped N terminus, which is buried in the catalytic pocket (Fig. 3a,b). In vivo,

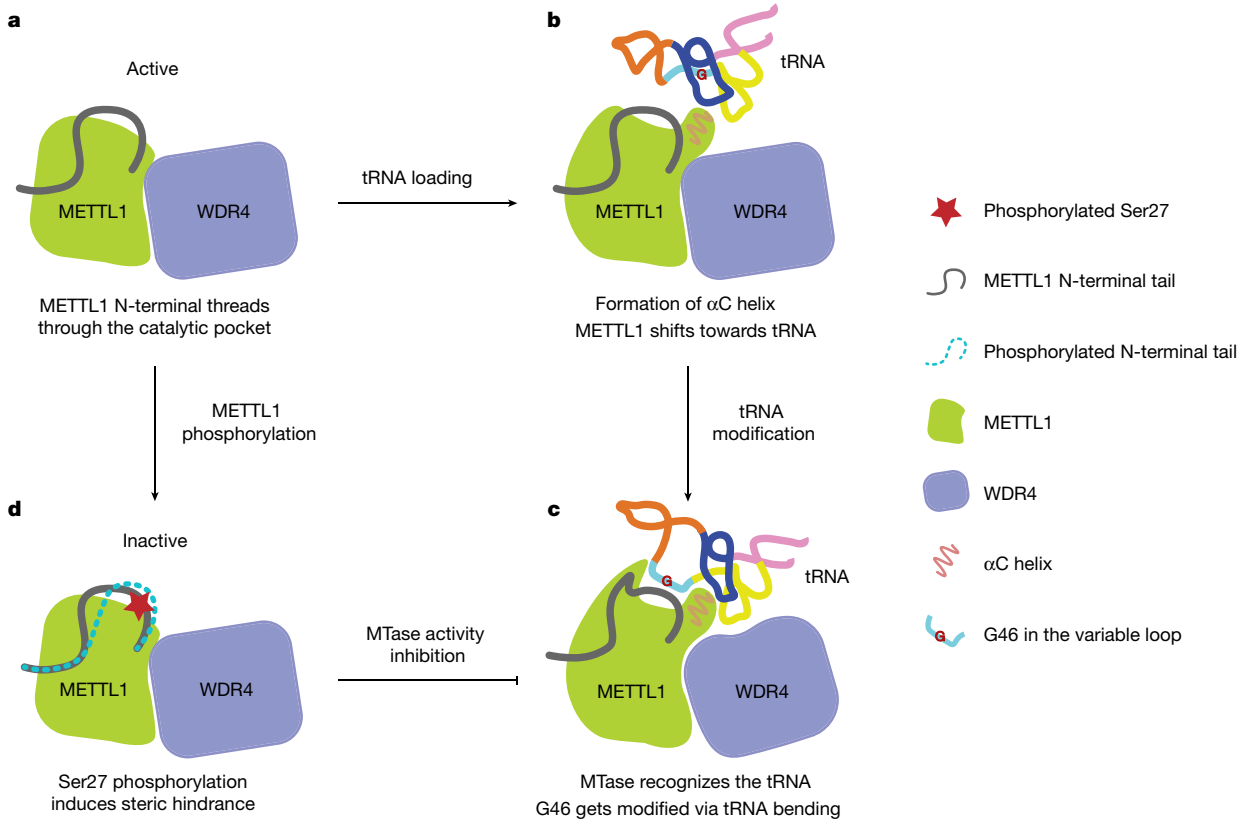


**Fig. 4 | Model of human METTL1–WDR4 in substrate recognition,) modification and catalytic regulation. a**, Cartoon representation of the METTL1–WDR4 complex with the U-shaped METTL1 N terminus that contributes to the catalytic pocket. **b**, tRNA loads to the METTL1–WDR4 platform with a specific binding mode. Upon tRNA binding, residues 164–173 of METTL1 form the αC helix, and METTL1 shifts towards the tRNA. **c**, METTL1–WDR4 recognizes tRNA with essential features, including the N-terminal tail, αC and α6 helices of METTL1 and B3–B4 of WDR4. tRNA undergoes bending to facilitate G46 flipping into the catalytic pocket to be modified. **d**, The N-terminal region (residues 24–27) of METTL shifts away when S27 is phosphorylated.

overexpression of S27D (to mimic S27 phosphorylation) METTL1 could not rescue $m^7G$ levels (Extended Data Fig. 8h). In the METTL1–WDR4–$tRNA^{Phe}$ structure, SAH was stabilized in the conserved *S*-adenosylmethionine (SAM)-binding pocket. The sulfur atom of SAH, where the methyl group should be in a SAM molecule, points into the catalytic pocket. A cluster of charged residues, D163, E240 and R109, is presented in the METTL1 catalytic pocket that is probably involved in the catalytic process (Fig. 3g and Extended Data Fig. 8i). S27 is in proximity to this cluster but does not directly interact with any of these residues. To understand the molecular mechanism by which S27 phosphorylation in the N-terminal region of METTL1 controls its catalytic activity, we made a series of amino acid substitutions to identify the determinants (charge and size) of METTL1 inactivation by phospho-S27 (Fig. 3h). Removing the hydroxyl group from the serine (S27A) showed comparable activity with the wild type. Side chains with similar lengths (S mutated to C or I) were tolerated, whereas negatively charged and phospho-mimetic (S27D), longer, and positively charged (S27K) and bulky aromatic (S27W) side chains, all inactivated METTL1. In our current model, METTL1 H26–S27 are in close proximity to the side chain of R109 on the α2 helix (Fig. 3i). Modelling shows that the phosphate group of phosphorylated S27 would clash with either the side chain of R109 (Fig. 3j) or the backbone of A21 on the D-arm of the tRNA (depending on the side-chain conformation). Therefore, we hypothesized that S27 phosphorylation induces steric hindrance, which results in the destabilization of the network of interactions among the N terminus, active site and the α2 helix. We tested this hypothesis by performing NMR assays with the S27D mutant of the N terminus, and indeed observed a specifically reduced interaction with residues 24–27 of METTL1 (Fig. 3k). The steric effect and possible rotamer conformations of phosphorylated S27 might place its phosphate group closer to the D-arm of tRNA (Fig. 3j). The introduction of the negative charge by phosphorylation might repel the tRNA and cause further local shifting of the N-terminal residues, to disrupt the catalytic centre and inhibit MTase activity dramatically.

To get molecular insight into the methylation mechanism of METTL1–WDR4, we modelled G46 alone in the catalytic pocket of METTL1 to allow for an $SN_2$-type nucleophilic reaction (Extended Data Fig. 8j). The N7 atom of G46 (attacking nucleophile) is co-linear with the S–$CH_3$ group of SAM (donor). Charged residues D163 and R109 potentially orient the target guanine proximal to the donor, whereas residues E240 and H26 can potentially interact with the G46 or neighbouring bases to facilitate the methyl transfer. In vitro assays showed that the MTase activity is not sensitive to lower pH buffer (pH less than 6.0) but is completely abolished by the H26A mutant. This suggests that H26 does not promote reaction chemistry as a proton shuttle in catalysis but is instead involved in the reaction process possibly by stabilizing a neighbouring base with its aromatic ring (Extended Data Fig. 8k,l). Together, these findings are highly consistent with a steric hindrance model to explain phosphorylation-mediated regulation of METTL1 activity, in which phosphorylated S27 locally disrupts the catalytic centre including METTL1 N-terminal residues 24–27 to prevent G46 methylation.

## Discussion

We present structures of the human METTL1–WDR4 heterodimer and in complex with tRNAs to provide molecular insights into substrate

recognition, modification and catalytic regulation by the $m^7G$ MTase complex. METTL1 and WDR4 form a heterodimer to provide a binding surface for their substrates. We reveal that METTL1 is the primary platform for tRNA binding and WDR4 serves as a supporting scaffold. The tRNA loading process involves the reconfiguration of METTL1 (Fig. 4a,b). Furthermore, we provide evidence that two α-helices cooperate with the METTL1 N-terminal region to recognize and facilitate bending of the tRNA for methylation (Fig. 4c). Finally, we identify the METTL1 N terminus as an essential feature of the catalytic pocket, and present a steric hinderance and charge-mediated model to explain regulation of MTase activity by METTL1 S27 phosphorylation (Fig. 4a,d).

A growing list of recent studies highlights the importance of METTL1–WDR4 oncogenic activity in many different cancer types, suggesting that inhibition of this MTase complex represents a promising new cancer therapeutic strategy. The mechanistic insights presented here will facilitate the design and development of anticancer drugs targeting METTL1–WDR4.

## Online content

Any methods, additional references, Nature Portfolio reporting summaries, source data, extended data, supplementary information, acknowledgements, peer review information; details of author contributions and competing interests; and statements of data and code availability are available at https://doi.org/10.1038/s41586-022-05566-4.


1. Roundtree, I. A., Evans, M. E., Pan, T. & He, C. Dynamic RNA modifications in gene expression regulation. *Cell* **169**, 1187–1200 (2017).
2. Frye, M., Harada, B. T., Behm, M. & He, C. RNA modifications modulate gene expression during development. *Science* **361**, 1346–1349 (2018).
3. Barbieri, I. & Kouzarides, T. Role of RNA modifications in cancer. *Nat. Rev. Cancer* **20**, 303–322 (2020).
4. Motorin, Y. & Helm, M. tRNA stabilization by modified nucleotides. *Biochemistry* **49**, 4934–4944 (2010).
5. Tomikawa, C. 7-Methylguanosine modifications in transfer RNA (tRNA). *Int. J. Mol. Sci.* **19**, 4080 (2018).
6. Alexandrov, A. et al. Rapid tRNA decay can result from lack of nonessential modifications. *Mol. Cell* **21**, 87–96 (2006).
7. Whipple, J. M., Lane, E. A., Chernyakov, I., D'Silva, S. & Phizicky, E. M. The yeast rapid tRNA decay pathway primarily monitors the structural integrity of the acceptor and T-stems of mature tRNA. *Genes Dev.* **25**, 1173–1184 (2011).
8. Alexandrov, A., Martzen, M. R. & Phizicky, E. M. Two proteins that form a complex are required for 7-methylguanosine modification of yeast tRNA. *RNA* **8**, 1253–1266 (2002).
9. Leulliot, N. et al. Structure of the yeast tRNA m7G methylation complex. *Structure* **16**, 52–61 (2008).
10. Orellana, E. A. et al. METTL1-mediated $m^7G$ modification of Arg-TCT tRNA drives oncogenic transformation. *Mol. Cell* **81**, 3323–3338.e14 (2021).
11. Dai, Z. et al. $N^7$-methylguanosine tRNA modification enhances oncogenic mRNA translation and promotes intrahepatic cholangiocarcinoma progression. *Mol. Cell* **81**, 3339–3355.e8 (2021).
12. Ma, J. et al. METTL1/WDR4-mediated m7G tRNA modifications and m7G codon usage promote mRNA translation and lung cancer progression. *Mol. Ther.* **29**, 3422–3435 (2021).
13. Han, H. et al. *N*7-methylguanosine tRNA modification promotes esophageal squamous cell carcinoma tumorigenesis via the RPTOR/ULK1/autophagy axis. *Nat. Commun.* **13**, 1478 (2022).
14. Chen, J. et al. Aberrant translation regulated by METTL1/WDR4-mediated tRNA *N*7-methylguanosine modification drives head and neck squamous cell carcinoma progression. *Cancer Commun.* **42**, 223–244 (2022).
15. Shaheen, R. et al. Mutation in WDR4 impairs tRNA $m^7G46$ methylation and causes a distinct form of microcephalic primordial dwarfism. *Genome Biol.* **16**, 210 (2015).
16. Braun, D. A. et al. Mutations in WDR4 as a new cause of Galloway–Mowat syndrome. *Am. J. Med. Genet. A* **176**, 2460–2465 (2018).
17. Trimouille, A. et al. Further delineation of the phenotype caused by biallelic variants in the WDR4 gene. *Clin. Genet.* **93**, 374–377 (2018).
18. Cartlidge, R. A. et al. The tRNA methylase METTL1 is phosphorylated and inactivated by PKB and RSK in vitro and in cells. *EMBO J.* **24**, 1696–1705 (2005).
19. Torres, A. G., Batlle, E. & de Pouplana, L. R. Role of tRNA modifications in human diseases. *Trends Mol. Med.* **20**, 306–314 (2014).
20. Suzuki, T. The expanding world of tRNA modifications and their disease relevance. *Nat. Rev. Mol. Cell Biol.* **22**, 375–392 (2021).
21. Pan, T. Modifications and functional genomics of human transfer RNA. *Cell Res.* **28**, 395–404 (2018).
22. Schimmel, P. The emerging complexity of the tRNA world: mammalian tRNAs beyond protein synthesis. *Nat. Rev. Mol. Cell Biol.* **19**, 45–58 (2018).
23. Lin, S. et al. Mettl1/Wdr4-mediated $m^7G$ tRNA methylome is required for normal mRNA translation and embryonic stem cell self-renewal and differentiation. *Mol. Cell* **71**, 244–255.e5 (2018).
24. Matsumoto, K. et al. RNA recognition mechanism of eukaryote tRNA (m7G46) methyltransferase (Trm8–Trm82 complex). *FEBS Lett.* **581**, 1599–1604 (2007).
25. Jumper, J. et al. Highly accurate protein structure prediction with AlphaFold. *Nature* **596**, 583–589 (2021).
26. Shi, H. & Moore, P. B. The crystal structure of yeast phenylalanine tRNA at 1.93 Å resolution: a classic structure revisited. *RNA* **6**, 1091–1105 (2000).
27. Blersch, K. F. et al. Structural model of the M7G46 methyltransferase TrmB in complex with tRNA. *RNA Biol.* **18**, 2466–2479 (2021).
28. Punjani, A., Rubinstein, J. L., Fleet, D. J. & Brubaker, M. A. cryoSPARC: algorithms for rapid unsupervised cryo-EM structure determination. *Nat. Methods* **14**, 290–296 (2017).



**Publisher's note** Springer Nature remains neutral with regard to jurisdictional claims in published maps and institutional affiliations.

Springer Nature or its licensor (e.g. a society or other partner) holds exclusive rights to this article under a publishing agreement with the author(s) or other rightsholder(s); author self-archiving of the accepted manuscript version of this article is solely governed by the terms of such publishing agreement and applicable law.

© The Author(s), under exclusive licence to Springer Nature Limited 2023

# Methods

### Cloning, protein expression and purification

The codon-optimized (*Escherichia coli* expression) full-length human *METTL1* and *WDR4* genes were synthesized from GENEWIZ and subcloned into a pETDuet-1 vector containing a $His_6$ tag at the N-terminal of WDR4. Mutated and truncated constructions were generated using Q5 site-directed mutagenesis kit (E0554S, NEB) or HiFi DNA assembly master mix (E2621S, NEB). The METTL1 and WDR4 proteins were co-expressed in *E. coli* Rosetta (DE3) cells (Sigma) that were induced with 0.5 mM isopropyl-1-thio-β-D-galactopyranoside (IPTG) at optical density at 600 nm ($OD_{600}$) = 0.6 at 16 °C overnight. Cells were harvested and sonicated in buffer containing 50 mM Tris-HCl, pH 8.0, 200 mM NaCl, 5% glycerol, 5 mM β-mercaptoethanol and 1 mM PMSF. The lysate was cleared by centrifugation and incubated with Ni Sepharose (Qiagen). The bound protein was eluted with buffer containing 200 mM imidazole and was further purified by combined Q column and heparin column (GE healthcare), and polished by size-exclusion chromatography (Superdex 200 Increase 10/300, GE Healthcare) in a buffer containing 50 mM Tris-HCl, pH 8.0, 150 mM NaCl and 1 mM Tris(2-carboxyethyl) phosphine hydrochloride (TCEP). Finally, the METTL1–WDR4 complex was concentrated to about 10 mg $ml^{-1}$ for EM and crystallization use.

### In vitro methylation assay

The tRNA probe (human $tRNA^{Val}TAC$) was synthesized (Horizon) as the following sequence: 5′-GGUUCCAUAGUGUAGCGGUUAUCAC GUCUGCUUUACACGCAGAAGgUCCUGGGUUCGAGCCCCAGUGGAAC CA-3′ (Extended Data Fig. 1b). The RNA probe was annealed at 95 °C for 5 min before reactions. The METTL1–WDR4 complex (wild type or variants) were purified by Ni-affinity chromatography. Optimized concentrations of the tRNA probe (100 nM) and METTL1–WDR4 (10 nM, wild type or variants) were applied to the reactions and followed the same protocol of a previous study[10]. In the MTase assay, testing the effects of buffer pH, the Tris buffer (pH 7.4) was substituted with sodium phosphate buffer (pH 5.6, 5.8, 6.0 and 7.4). Scintillation signals were measured using the Tri-Carb 2910 TR instrument (Perkin Elmer).

### Size-exclusion co-migration assay

The METTL1–WDR4 complex was incubated with $tRNA^{Phe}$ (R4018, Sigma) and SAH, or with $tRNA^{Val}$ (synthetic RNA, Horizon) and SAM at room temperature for 1 h. The molar ratio of protein, tRNA and compound was 1:1.4:1.5. Incubated ternary complex samples, the METTL1–WDR4 binary complex and tRNA were applied to a Superdex 200 Increase 10/300 (GE Healthcare) separately. Peak fractions were analysed by native PAGE and stained with EB and G250 to visualize the tRNA and protein complex, respectively.

### TR-FRET assay

The purified full-length METTL1–WDR4 complex was labelled with BODIPY (D2184, Thermo Fisher) as described previously[29]. $tRNA^{Val}$ was labelled with biotin by 5′ EndTag DNA/RNA Labeling Kit (MB-9001, Vector) according to the vendor's procedures.

In the competitive assay, dilution of unlabelled apo METTL1, full-length or truncated METTL1–WDR4 was added to assay mix with final concentrations of 2 nM Tb-strep, 10 nM tRNA–biotin, 40.5 nM BODIPY–METTL1–WDR4, 121.5 nM SAM and 100 nM nonspecific RNA in a buffer containing 50 mM Tris-HCl, pH 8.0, 150 mM NaCl and 1 mM TCEP. TR-FRET assays were performed in 384-well microplates (4514, Corning) with a final assay volume of 15 µl. Before TR-FRET measurements were conducted, the reactions were incubated for 15 min. After excitation of terbium fluorescence at 337 nm, emissions at 490 nm (terbium) and 520 nm (BODIPY) were recorded with a 70-µs delay over 130 µs to reduce background fluorescence, and the reaction was followed over more than 20 or more than 100-s cycles of each data point using a PHERAstar microplate reader (BMG Labtech Model FS). The TR-FRET signal of each data point was extracted by calculating the 520:490 nm ratio. Statistical calculations were performed using Prism 8.0.2.

### Crystallization, data collection and structure determination

The recombinant METTL1–WDR4 complex was incubated with threefold molar excess of SAM and further purified by Superdex 200 Increase 10/300 column (GE Healthcare). The sample was concentrated to 10 mg $ml^{-1}$ for crystallization. Crystals of the METTL1–WDR4 complex were obtained by mixing 75 nl complex solution and 75 nl of reservoir solution using an NT8 (Formulatrix), and were grown by the sitting drop vapour diffusion method at 20 °C. Crystals of the METTL1–WDR4 complex were grown from 2 M $(NH_4)_2SO_4$, 0.2 M K–Na tartrate, 0.1 M $Na_3$ citrate pH 6.5 for 3 weeks. All crystals were cryo-protected using corresponding reservoir buffers supplemented with 20% ethylene glycol and flash frozen in liquid nitrogen. All diffraction datasets were collected at APS Chicago on beamlines 24-ID-C and 24ID-E at 100K. Data were indexed and integrated using RAPS pipeline from APS Chicago[30]. A 3.1 Å resolution dataset was collected at a wavelength of 0.97918 Å. The phases of the METTL1–WDR4 structure was solved by molecular replacement using the program Phenix[31]. The METTL1 (PDB 3CKK) and WDR4 (originating from chain D of the Trm8–Trm82 complex; PDB 2VDU) were used as separate search models. The model was adjusted using Coot, and structure refinement was performed using Phenix and autoBUSTER (version 2.10.4). The Ramachandran plot shows that 93.89% of residues are in favoured regions, with the remaining in allowed regions. In the final coordinate file of 7U20, residues 34–56 and 75–265 of METTL1, and residues 0–44 (residue 0 is from the protein tag) and 60–348 of WDR4 are modelled. All statistics of data processing and structure refinement of the METTL1–WDR4 complex are summarized in Extended Data Table 1. The structure figures were prepared using PyMOL, and model quality was assessed with MOLPROBITY (version 4.2)[32]. Structural biology applications used in this project were compiled and configured by SBGrid[33].

### EM sample preparation and data collection

The METTL1–WDR4–$tRNA^{Phe}$ complex was reconstituted by incubating METTL1–WDR4, $tRNA^{Phe}$ (R4018, Sigma) and SAH at the molar ratio of 1:1.2:1.5 at room temperature for 1 h. The ternary complex was further purified on a Superdex 200 Increase 10/300 column (GE Healthcare) in buffer containing 50 mM Tris-HCl, pH 8.0, 150 mM NaCl and 1 mM TCEP. Samples used for EM were measured for a final absorbance of 0.2–1.0 using a Nanodrop spectrophotometer. The METTL1–WDR4–$tRNA^{Val}$ complex was reconstituted by incubating METTL1–WDR4, annealled $tRNA^{Val}$ (synthetic RNA, Horizon) and SAM, in the same conditions as above. Both samples were checked for morphology and homogeneity using negative-staining EM. For each ternary complex, 2.5 µl sample (absorbance at 280 nm = 0.05) was placed on a glow-discharged carbon film copper grid (CF-400CU, Electron Microscopy Sciences). After a 60-s incubation, the grid was stained in 2% uranyl formate for 30 s, air dried and imaged on a Tecnai G2 Spirit BioTWIN microscope at Harvard Medical School Electron Microscopy Facility.

A 3-µl drop of the METTL1–WDR4–tRNA complex was applied to glow-discharged Quantifoil R1.2/1.3 400 mesh copper grids (Electron Microscopy Sciences). The grids were blotted for 4 s in 100% humidity at 4 °C and plunge-frozen using the FEI Vitrobot Mark IV. Cryo-EM data collection of the METTL1–WDR4–$tRNA^{Phe}$ complex was performed on a 300 keV Titan Krios microscope (FEI) with a K3 direct electron detector (Gatan) using Latitude-S (Gatan Microscopy Suites software package MODEL 700.LS.731) at the National Cancer Institute's National Cryo-EM Facility. For the initial dataset, 5,990 videos were collected in counting mode, with 40 frames per video, 3.6-s exposure time, 60 $e^{-}$ $Å^{-2}$ accumulated dose and 1.08 Å pixel size. For the final dataset, 10,415 videos were collected in counting mode, with 40 frames per video, 3.4-s exposure time, 50 $e^{-}$ $Å^{-2}$ accumulated dose and 1.08 Å pixel size.

Cryo-EM data collection of the METTL1–WDR4–tRNA$^{Val}$ complex was performed on a 300 keV Titan Krios microscope (FEI) with a K3 direct electron detector (Gatan) using SerialEM (version 3.8.5) at the Harvard Center for Cryo-Electron Microscopy (HC2EM). Videos ($n$ = 5,095) were collected in counting mode, with 50 frames per video, 1.5-s exposure time, 51.8 $e^{-}$ Å$^{-2}$ accumulated dose and 0.825 Å pixel size.

### Cryo-EM data processing and model building

For initial dataset for METTL1–WDR4–tRNA$^{Phe}$, videos were motion-corrected using MotionCor2 (ref. [34]). Patch contrast transfer function estimation was performed using cryoSPARC[28]. Particles were initially picked using blob picker in cryoSPARC and subjected to 2D classification. Selected classes representing the ternary complex only accounted for approximately 3% of the total particles and are used for ab initio 3D reconstruction to generate a reference model. For the final dataset for METTL1–WDR4–tRNA$^{Phe}$, 10,415 videos were collected. Motion correction and contrast transfer function estimation were performed in the same way as in the initial dataset. Supervised particle picking was carried out using the trained model from dataset I in Topaz[35]. After 2D classification, 634,274 particles were selected for ab initio 3D reconstruction followed by 3D classification (heterogeneous refinement). Of the particles, 28% were the binary complex without the tRNA and were used to reconstruct a 3.5 Å cryo-EM map. Two 3D classes of the METTL1–WDR4–tRNA$^{Phe}$ ternary complex (51% of the particles) were selected for another round of 2D classification to remove bad particles. After Bayesian polishing (Relion)[36] and non-uniform 3D refinement (cryoSPARC)[37], the map resolution of the METTL1–WDR4–tRNA$^{Phe}$ ternary complex reached 3.3 Å. For METTL1–WDR4–tRNA$^{Val}$, 5,094 videos were collected. The image processing procedures were the same as for the METTL1–WDR4–tRNA$^{Phe}$ dataset, with the exception that no binary complex class was found after 3D classification. Of the particles, 31% were selected for Bayesian polishing and non-uniform 3D refinement, yielding a map with a resolution of 3.6 Å. 3D variability analysis of METTL1–WDR4–tRNA$^{Phe}$ were carried out in cryoSPARC[38] based on the non-uniform refinement, with the low-pass filter set at 5 Å and the number of modes set to 3 (Extended Data Fig. 2a). Each of the three components from 3D variability analysis represent a certain motion that contribute to the data variability. A video of component 1 that represents the tRNA melting was generated (Supplementary Video 1). Particles were clustered into four groups based on the principle components and all four groups were subjected to 3D refinement (Extended Data Fig. 2a). The cryo-EM map of METTL1–WDR4–tRNA$^{Phe}$ is auto-sharpened by NU-refinement in CryoSPARC with a B-factor of −125.3. The sharpening B-factor for the cryo-EM map of METTL1–WDR4–tRNA$^{Val}$ is −147.8. In both METTL1–WDR4–tRNA$^{Phe}$ and METTL1–WDR4–tRNA$^{Val}$ maps, we observed some degree of variations in local and directional resolutions, which could be explained by flexibility and preferred orientations[39] (Extended Data Fig. 2c–h). Consequently, ambiguous densities are present in a few regions of the sharpened maps. To overcome these limitations, DeepEMhancer was used to post-process the cryo-EM maps of METTL1–WDR4–tRNA$^{Phe}$ and METTL1–WDR4–tRNA$^{Val}$ to facilitate model building[40]. The initial model of METTL1–WDR4 was generated by rigid body fitting of the METTL1–WDR4 crystal structure model into the cryo-EM maps using ChimeraX[41]. The N-terminal region (residues 26–33) of METTL1 was modelled based on AlphaFold prediction in agreement with weak density and refined restrained to the conformation of the prediction. The tRNA$^{Phe}$ was modelled using a yeast tRNA$^{Phe}$ (PDB 1EHZ). tRNA$^{Val}$ was homology modelled using a rabbit tRNA$^{Val}$ (PDB 3JAG, chain 2). Inspection, model building and manual adjustments were carried out in Coot[42]. Real-space refinements were performed using Phenix[31]. The crystal structures and AlphaFold-predicted METTL1 N-terminal region (residues 1–33) were used as reference model restraints in Phenix refinements. For the final coordinate file of 8CTH (METTL1–WDR4–tRNA$^{Phe}$), residues 26–54 and 76–262 of METTL1, residues 6–28, 36–43, 62–233 and 244–318 of WDR4, nucleotides 1–74 of tRNA$^{Phe}$ and cofactor SAH are modelled. For the final coordinate file of 8CTI (METTL1–WDR4–tRNA$^{Val}$), residues 34–54, 77–125 and 131–262 of METTL1, residues 13–28, 62–233 and 244–318 of WDR4, and nucleotides 1–16 and 18–71 of tRNA$^{Val}$ are modelled. All statistics of data processing and structure refinement of cryo-EM structures are summarized in Extended Data Table 1. All representations of densities and structural models were generated using Chimera, ChimeraX and PyMOL Molecular Graphics System, version 2.0 Schrödinger, LLC.

### Rescue experiments

Mouse *Mettl1*-KO R1/E embryonic stem cells from a previous study[23] were used for METTL1 rescue experiments. In the case of WDR4 rescue experiments, new *Wdr4* KO were generated from mouse R1/E embryonic stem cells (a gift from L. Wu, SCRC-1036, American Type Culture Collection) following our previous protocol[23] and verified by immunoblotting or PCR genotyping. All cells were frequently checked by their morphological features and functions. No other authentication was performed. All cell lines were tested to be mycoplasma-negative. KO cell lines were cultured in serum/LIF medium (DMEM (Gibco) with 1,000 u ml$^{-1}$ mouse LIF (Gemini), 15% stem cell FBS (Gemini), 1× sodium pyruvate (Gibco), 1× NEAA (Gibco), 1× L-glutamine (Gibco), 50 μM 2-mercaptoethanol (Thermo Fisher) and 1% penicillin–streptomycin (Gibco)) in a 5% $CO_2$ cell culture incubator at 37 °C. Cells were cultured in a feeder-free condition in gelatin-coated dishes (0.1% gelatin solution for 30 min at 37 °C) to enhance cell attachment. For rescue experiments, cells were first washed with PBS twice and then trypsinized (0.1% trypsin in PBS) at 37 °C for 3 min. Cells were then resuspended in serum/LIF medium and counted. Then, the METTL1, WDR4 or empty vector plasmids (10 μg) were transfected into mouse embryonic stem cells (approximately $4 \times 10^6$ cells) using the reverse transfection method with Lipofectamine 2000 (20 μl; Invitrogen). Cell media were replaced daily and cells were collected 48 h post-transfection and split into two for RNA and protein isolation, respectively.

### Northwestern blot and western blot

For northwestern blot, 10 μg total RNA samples were mixed with 2× TBE loading buffer (Bio-Rad) and incubated at 95 °C for 5 min. The samples were then loaded into 15% TBE–urea (Bio-Rad) gels to separate the RNAs by molecular weight. Next, the RNAs were transferred onto a positive charged nylon membrane and crosslinked with UV. Next, membranes were immunoblotted with mouse monoclonal anti-m$^7$G (clone 4141-13, 1:1,000; RN017M, MBL International) and detected using the enhanced chemiluminescence (ECL) method. For loading control, the membrane was then blotted with radioactive labelled probes against U6 small nuclear RNA. Blotted membranes were exposed to autoradiography films. For western blotting, cell pellets were resuspended in passive lysis buffer (Promega), supplemented with protease inhibitors (complete, Roche). Protein concentrations were assessed by Bradford assay (5000006, Bio-Rad) and an equal amount of protein was loaded per lane. Before loading, the samples were supplemented with SDS–PAGE sample buffer and β-mercaptoethanol was added to each sample. Of protein, 10–40 μg was separated on SDS–PAGE gels (4–20%), and blotted onto nitrocelullose membranes (Thermo Fisher). Membranes were then immunoblotted with the following antibodies: β-actin (1:10,000; ab8229, Abcam), METTL1 (1:2000; 14994-1, Proteintech) and WDR4 (clone EPR11052, 1:2,000; ab169526, Abcam). Membranes were imaged using the Odyssey Imaging System, Image Studio (Li-Cor, version 5.2.5).

### AlphaFold prediction

Full-length sequences of human METTL1 and WDR4 were input into AlphaFold 2.2 with Amber refinement[25]. To assess the position of WDR4 relative to METTL1, AlphaFold was run in the ptm mode, and the expected position error between the two proteins was extracted. An expected error of less than 5 Å was used as the criterion to determine

interaction. Low-confidence regions (plDDT < 70), including the glycine linker, were removed to obtain the final model.

### NMR spectroscopy

NMR experiments were conducted on Avance III Bruker (version 3.4) spectrometers operating at 600 and 800 MHz, equipped with three-channel $^{1}H$, $^{13}C$, $^{15}N$ cryogenically cooled probes. If not stated otherwise, the experimental temperature was set to 15 °C. Data were processed using NmrPipe[43] and analysed using CCPNmr Analysis[44]. A sample of 420 mM $^{15}N^{13}C$-labelled METTL1 1–75 was prepared in 50 mM NaPi pH = 6.0, 100 NaCl, 1 mM TCEP and 5% v/v $^{2}H_2O$ for backbone assignments. The assignment routine used regular HSQC, HNCA, HN(CO)CA, HNCO, HN(CA)CO, HN(CA)CB and CBCA(CO)NH experiments. All 3D experiments were set up with 10% non-uniform sampling using Poisson gap sampling[45] and reconstructed using the hmsIST protocol[46]. Of non-proline residues, 91% were assigned. Chemical shift assignments have been deposited in the Biological Magnetic Resonance Data Bank under accession number 51362. Secondary structure predictions were obtained from the Talos-N algorithm[47] and proved that most of the construct is disordered, except for the 46–55 segment, which exhibits 40–70% secondary structure (in line with the presence of a short β-strand in some crystal structures). Assignments were readily transferred to the S27D mutant. Given the impossibility to express a truncated construct of METTL1 for direct interaction studies, we utilized a competition assay in which $^{15}N$-labelled METTL1 1–75 competes off the N terminus of unlabelled METTL1. Samples of 23, 46 and 92 mM METTL1 1–75 were measured with and without 230 mM of unlabelled full-length METTL1, corresponding to 0, 2.5, 5 and 10 molar equivalents. A SOFAST-HMQC experiment with a recycle delay of 0.2 s was used for accelerated sampling. Titration experiments showed line broadening of a subset of peaks, which indicates a slow-exchange binding mode on the NMR timescale. Owing to the nature of the assay and the use of SOFAST, measurement of peak intensities is not quantitative; however, this allows mapping of the interaction onto the 1–75 fragment. To validate our NMR results in physiological conditions, we reproduced our competition assay at pH 7.4 and at both 15 °C and 25 °C. Eight peaks disappeared from the spectrum due to a faster exchange rate of amide protons with water, including residues 26–28. This impaired our ability to assess binding in a semi-quantitative way; however, evidence of binding of the 18–27 segment is present. pH does not seem to impact binding affinity, and higher temperature seems to weaken the affinity but by a small percentage.

### Statistics and reproducibility

For the rescue experiment, the $m^7G$ level and protein expression level of all samples were checked by northwestern blot and western blot, respectively. Blots are representative of two biological independent experiments. For the analysis of protein complexes using SDS–PAGE and native PAGE, each experiment was repeated independently at least two times with similar results.

### Reporting summary

Further information on research design is available in the Nature Portfolio Reporting Summary linked to this article.

## Data availability

The cryo-EM structures of METTL1–WDR4–$tRNA^{Phe}$ and METTL1–WDR4–$tRNA^{Val}$, and X-ray crystal structure of METTL1–WDR4 have been deposited to the PDB under accession numbers 8CTH, 8CTI and 7U20, respectively. The cryo-EM density maps of METTL1–WDR4–$tRNA^{Phe}$ and METTL1–WDR4–$tRNA^{Val}$ have been deposited in the Electron Microscopy Data Bank under accession numbers 26990 and 26991. Several structural coordinates in the PDB database were used in this study, which can be located through accession numbers 1EHZ, 2VDU, 3JAG, 3CKK, 7OGJ, 2VDV and 7PL1. NMR resonance assignments were deposited to the Biological Magnetic Resonance Data Bank under accession number 51362.


29. Yue, H. et al. Rapid 'mix and read' assay for scalable detection of SARS-CoV-2 antibodies in patient plasma. Preprint at *medRxiv* https://doi.org/10.1101/2020.09.01.20184101 (2020).
30. Kabsch, W. Xds. *Acta Crystallogr. D Biol. Crystallogr.* **66**, 125–132 (2010).
31. Liebschner, D. et al. Macromolecular structure determination using X-rays, neutrons and electrons: recent developments in Phenix. *Acta Crystallogr. D Struct. Biol.* **75**, 861–877 (2019).
32. Chen, V. B. et al. MolProbity: all-atom structure validation for macromolecular crystallography. *Acta Crystallogr. D Biol. Crystallogr.* **66**, 12–21 (2010).
33. Morin, A. et al. Cutting edge: collaboration gets the most out of software. *eLife* **2**, e01456 (2013).
34. Zheng, S. Q. et al. MotionCor2: anisotropic correction of beam-induced motion for improved cryo-electron microscopy. *Nat. Methods* **14**, 331–332 (2017).
35. Bepler, T. et al. Positive-unlabeled convolutional neural networks for particle picking in cryo-electron micrographs. *Nat. Methods* **16**, 1153–1160 (2019).
36. Zivanov, J., Nakane, T. & Scheres, S. H. A Bayesian approach to beam-induced motion correction in cryo-EM single-particle analysis. *IUCrJ* **6**, 5–17 (2019).
37. Punjani, A., Zhang, H. & Fleet, D. J. Non-uniform refinement: adaptive regularization improves single-particle cryo-EM reconstruction. *Nat. Methods* **17**, 1214–1221 (2020).
38. Punjani, A. & Fleet, D. J. 3D variability analysis: resolving continuous flexibility and discrete heterogeneity from single particle cryo-EM. *J. Struct. Biol.* **213**, 107702 (2021).
39. Aiyer, S., Zhang, C., Baldwin, P. R. & Lyumkis, D. in *CryoEM* (eds. Gonen, T. & Nannenga, B. L.) 161–187 (Springer, 2021).
40. Sanchez-Garcia, R. et al. DeepEMhancer: a deep learning solution for cryo-EM volume post-processing. *Commun. Biol.* **4**, 874 (2021).
41. Pettersen, E. F. et al. UCSF ChimeraX: structure visualization for researchers, educators, and developers. *Protein Sci.* **30**, 70–82 (2021).
42. Emsley, P., Lohkamp, B., Scott, W. G. & Cowtan, K. Features and development of Coot. *Acta Crystallogr. D Biol. Crystallogr.* **66**, 486–501 (2010).
43. Delaglio, F. et al. NMRPipe: a multidimensional spectral processing system based on UNIX pipes. *J. Biomol. NMR* **6**, 277–293 (1995).
44. Vranken, W. F. et al. The CCPN data model for NMR spectroscopy: development of a software pipeline. *Proteins Struct. Funct. Bioinf.* **59**, 687–696 (2005).
45. Hyberts, S. G., Takeuchi, K. & Wagner, G. Poisson-gap sampling and forward maximum entropy reconstruction for enhancing the resolution and sensitivity of protein NMR data. *J. Am. Chem. Soc.* **132**, 2145–2147 (2010).
46. Hyberts, S. G., Milbradt, A. G., Wagner, A. B., Arthanari, H. & Wagner, G. Application of iterative soft thresholding for fast reconstruction of NMR data non-uniformly sampled with multidimensional Poisson gap scheduling. *J. Biomol. NMR* **52**, 315–327 (2012).
47. Shen, Y. & Bax, A. Protein backbone and sidechain torsion angles predicted from NMR chemical shifts using artificial neural networks. *J. Biomol. NMR* **56**, 227–241 (2013).



**Acknowledgements** E.A.O. is supported by the Pew Latin American Fellows Program in the Biomedical Sciences from Pew Charitable Trusts and by a fellowship from the Damon Runyon Cancer Research Foundation (DRG-2378–19). R.I.G. is supported by an Outstanding Investigator Award (R35CA232115) from the National Cancer Institute of the US National Institutes of Health. This work was in part supported by National Institutes of Health grants R01 CA218278 and R01 CA214608 (to E.S.F.), the Mark Foundation for Cancer Research (Mark Foundation Emerging Leader Award 19-001-ELA to E.S.F.) and the Cancer Research Institute (Irvington Postdoctoral Fellowship CRI 3442 to S.S.R.B.). This research was, in part, supported by the National Cancer Institute's National Cryo-EM Facility at the Frederick National Laboratory for Cancer Research under contract HSSN261200800001E. We thank the staff at the Harvard Cryo-EM Center for Structural Biology for their support during grid screening and data collection. This research used resources of the Advanced Photon Source, a US Department of Energy Office of Science User Facility operated for the Department of Energy Office of Science by Argonne National Laboratory under contract number SE-AC02-06CH11357. We acknowledge the SBGrid consortium for assistance with high-performance computing.


**Author contributions** J.L. and R.I.G. conceived the project. J.L. performed recombinant protein purification and ternary complex reconstitution. J.L., L.W. and P.F. prepared and optimized samples for cryo-EM. L.W. performed cryo-EM data processing. J.L. built models, with assistance from L.W., S.S.R.B. and M.H. J.L., R.P.N. and E.S.F. determined and refined the crystal structure of the binary complex. J.L., Q.H., T.V. and H.Y. performed biochemical experiments. E.A.O., J.L. and Q.H. performed cellular experiments. R.I.G., E.S.F., H.A. and H.W. supervised the project. All authors organized and analysed the data. J.L., L.W. and R.I.G. wrote the manuscript with input from all authors.

**Competing interests** R.I.G. is a co-founder and scientific advisory board (SAB) member of 28/7 Therapeutics and Theonys. E.S.F. is a founder, SAB member and equity holder in Civetta Therapeutics, Lighthorse Therapeutics, Neomorph, Inc. (board of directors) and Proximity Therapeutics. E.S.F. is a SAB member and equity holder in Avilar Therapeutics and Photys Therapeutics. E.S.F. is also a consultant to Novartis, Sanofi, EcoR1 capital, Avilar and Deerfield. The Fischer laboratory receives or has received research funding from Astellas, Novartis, Voronoi, Interline, Ajax and Deerfield. The rest of the authors declare no competing interests.

**Additional information**


**Supplementary information** The online version contains supplementary material available at https://doi.org/10.1038/s41586-022-05566-4.



**Correspondence and requests for materials** should be addressed to Richard I. Gregory.



**Peer review information** *Nature* thanks Hauke Hillen and the other, anonymous, reviewer(s) for their contribution to the peer review of this work.



**Reprints and permissions information** is available at http://www.nature.com/reprints.

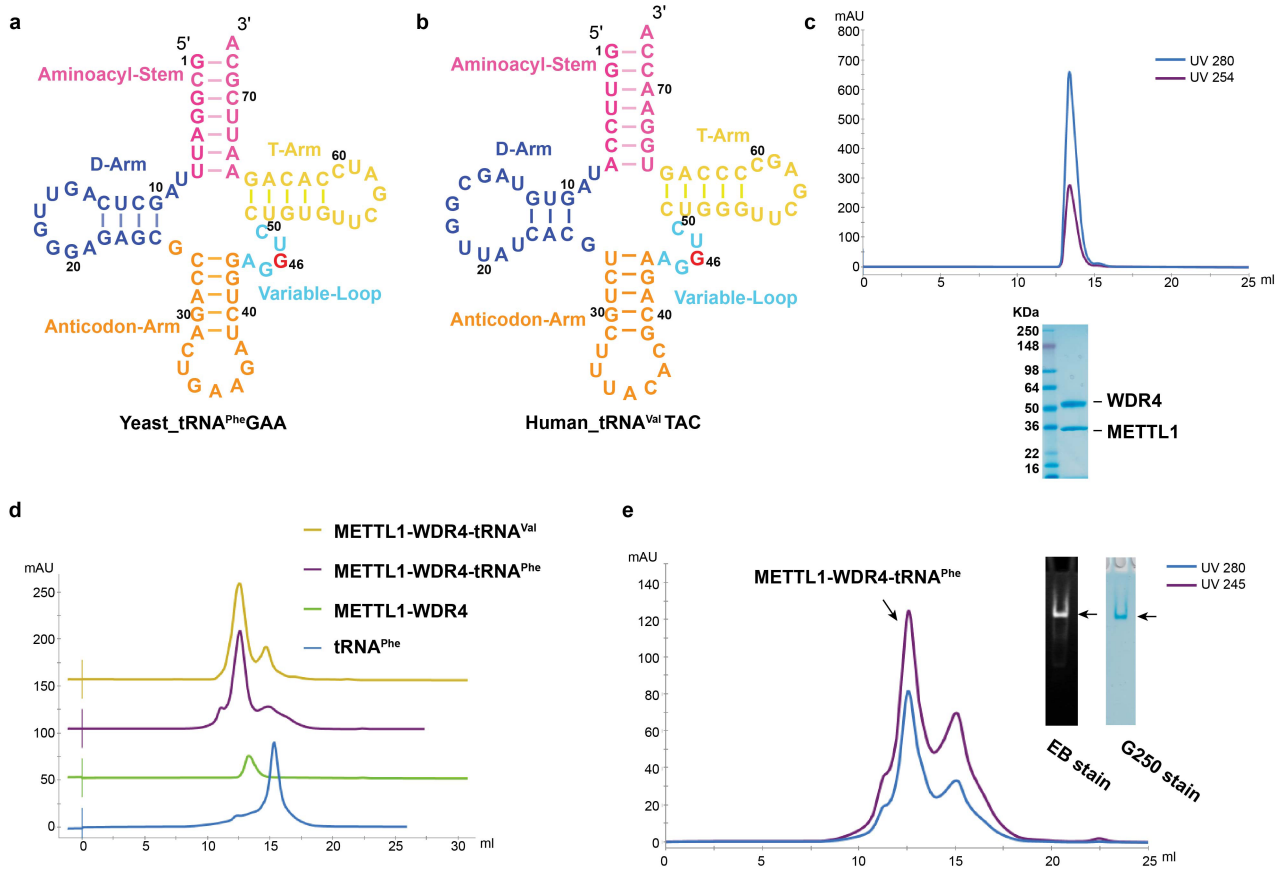


**Extended Data Fig. 1 | Sample preparation and quality check.** (**a**–**b**) tRNA candidates for ternary complex reconstitution. Schematic representations of yeast tRNA$^{Phe}$ and human tRNA$^{Val}$. Yeast tRNA$^{Phe}$ is a matured tRNA$^{Phe}$ purified from yeast (Sigma) (**a**). Human tRNA$^{Val}$ is an annealed single strand RNA oligos synthesized based on human tRNA$^{Val}$-TAC sequence (Horizon) (**b**). (**c**) Chromatography traces and SDS-PAGE analysis of purified METTL1-WDR4 complex (absorption at 280nm and 254nm). For gel source data, see Supplementary Fig. 3. (**d**) Gel filtration profiles of free tRNA$^{Phe}$ (blue), METTL1-WDR4 binary complex (green), METTL1-WDR4-tRNA$^{Phe}$ ternary complex (purple) and METTL1-WDR4-tRNA$^{Val}$ ternary complex (yellow) (absorption at 280nm are shown). (**e**) Identification of the reconstituted METTL1-WDR4-tRNA$^{Phe}$ ternary complex. Sample in the main peak of the reconstitution chromatography trace is analyzed by native PAGE. tRNA and protein are virtualized by EB and G250 staining separately. For gel source data, see Supplementary Fig. 4.

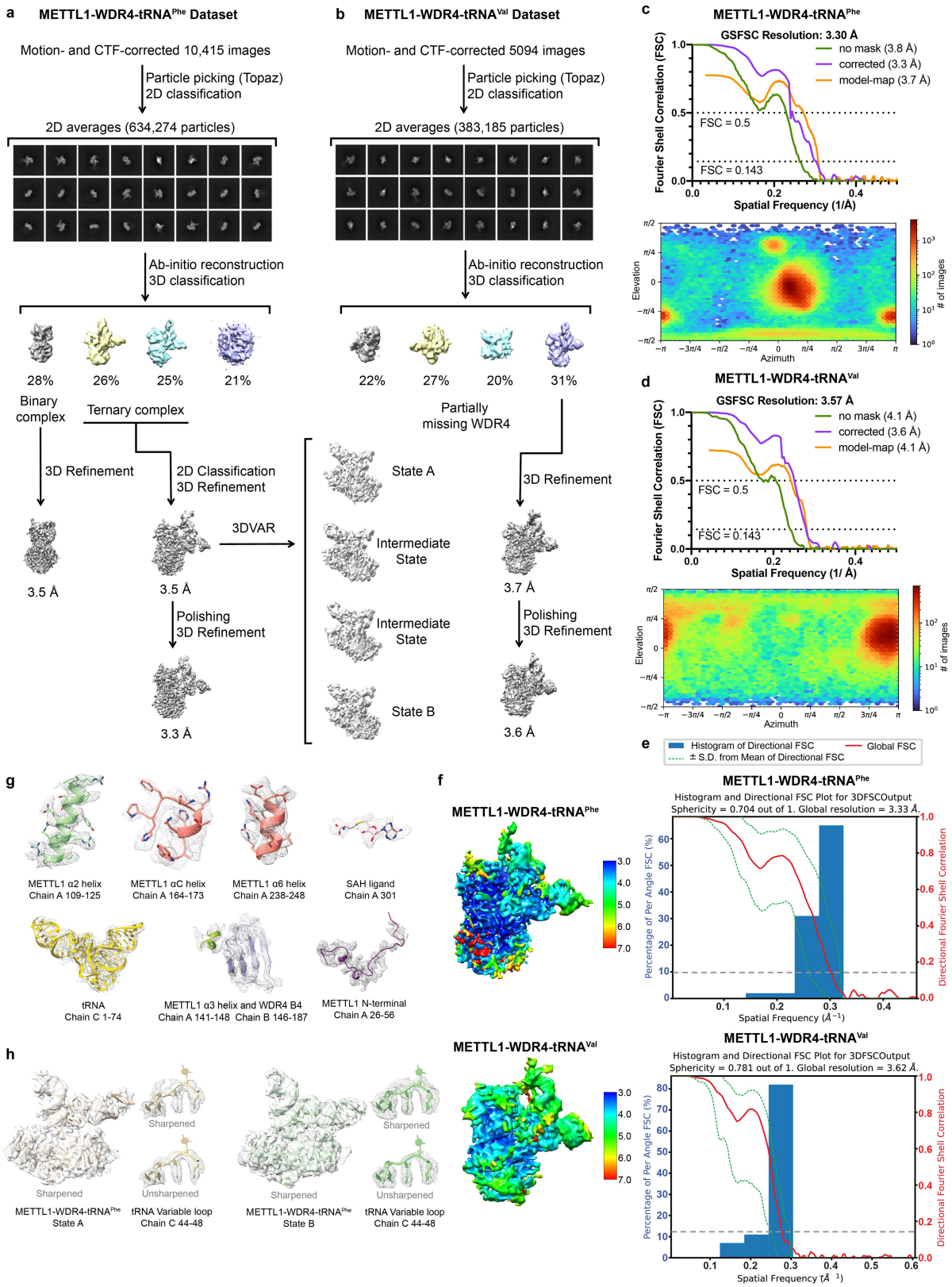


**Extended Data Fig. 2 | Cryo-EM workflows and the quality of reconstructed cryo-EM maps.** (**a**–**b**) Workflow of 3D reconstruction of METTL1-WDR4-tRNA$^{Phe}$ dataset (**a**) and the METTL1-WDR4-tRNA$^{Val}$ dataset (**b**). (**c**–**d**) Fourier shell correlation (FSC) curves (upper panel) and orientation distributions (lower panel) of 3D reconstructed METTL1-WDR4-tRNA$^{Phe}$and METTL1-WDR4-tRNA$^{Val}$ cryo-EM maps. See also Extended Data Table 1. (**e**) Histogram of directional FSC curves of METTL1-WDR4-tRNA$^{Phe}$ dataset (upper panel) and the METTL1-WDR4-tRNA$^{Val}$ dataset (lower panel). (**f**) Local resolutions of METTL1-WDR4-tRNA$^{Phe}$ (upper panel) and METTL1-WDR4-tRNA$^{Val}$ (lower panel) cryo-EM maps. (**g**) Representative segments of sharpened cryo-EM map fitted with the model. (**h**) State A and State B models of METTL1-WDR4-tRNA$^{Phe}$ fit in sharpened cryo-EM maps. The variable loop of tRNA fitted with sharpened (top) and unsharpened (bottom) maps from 3D variability analysis are shown in parallel with the whole model.

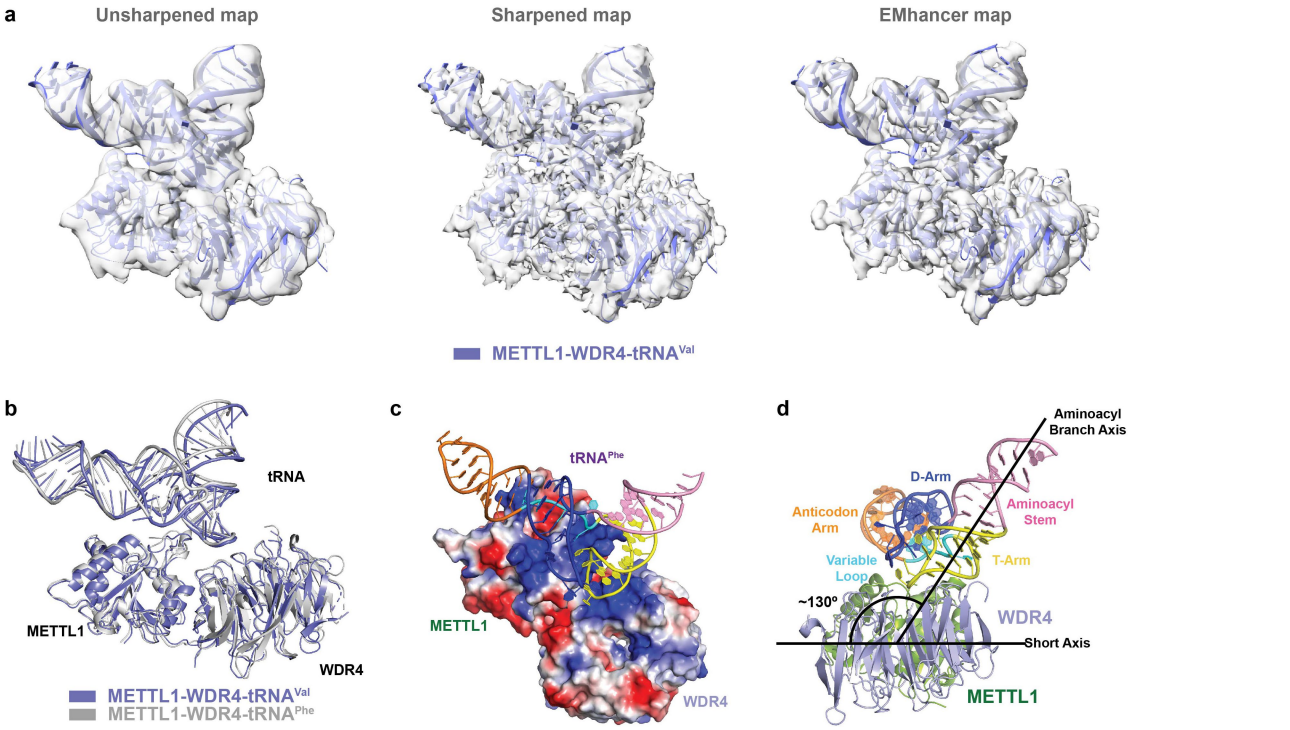


**Extended Data Fig. 3 | Similar binding mode of METTL1-WDR4 to tRNA$^{Phe}$ and tRNA$^{Val}$.** (**a**) Cryo-EM density maps of METTL1-WDR4-tRNA$^{Val}$ complex and the corresponding atomic model. The unsharpened (left), sharpened (middle) and DeepEMhancer processed (right) density maps are shown. (**b**) Overall structural superposition of METTL1-WDR4-tRNA$^{Val}$ (slate) and METTL1-WDR4-tRNA$^{Phe}$ (white). (**c**) Electrostatic potential of METTL1 and WDR4 in ternary complex (tRNA$^{Phe}$). Red, negative; blue, positive. Figure was generated using PyMOL. tRNA domains are colored according to Extended Data Fig. 1a. (**d**) Tilted loading of tRNA$^{Phe}$ onto the METTL1-WDR4 complex. Overall structure of METTL1-WDR4-tRNA$^{Phe}$ complex from the WDR4 side. The angle between the short axis of METTL1-WDR4 and the aminoacyl-branch axis of tRNA is about 130 degrees. The angle is measured utilizing residue 213 (WDR4), residue 163 (WDR4) and base 73 of tRNA using PyMOL.

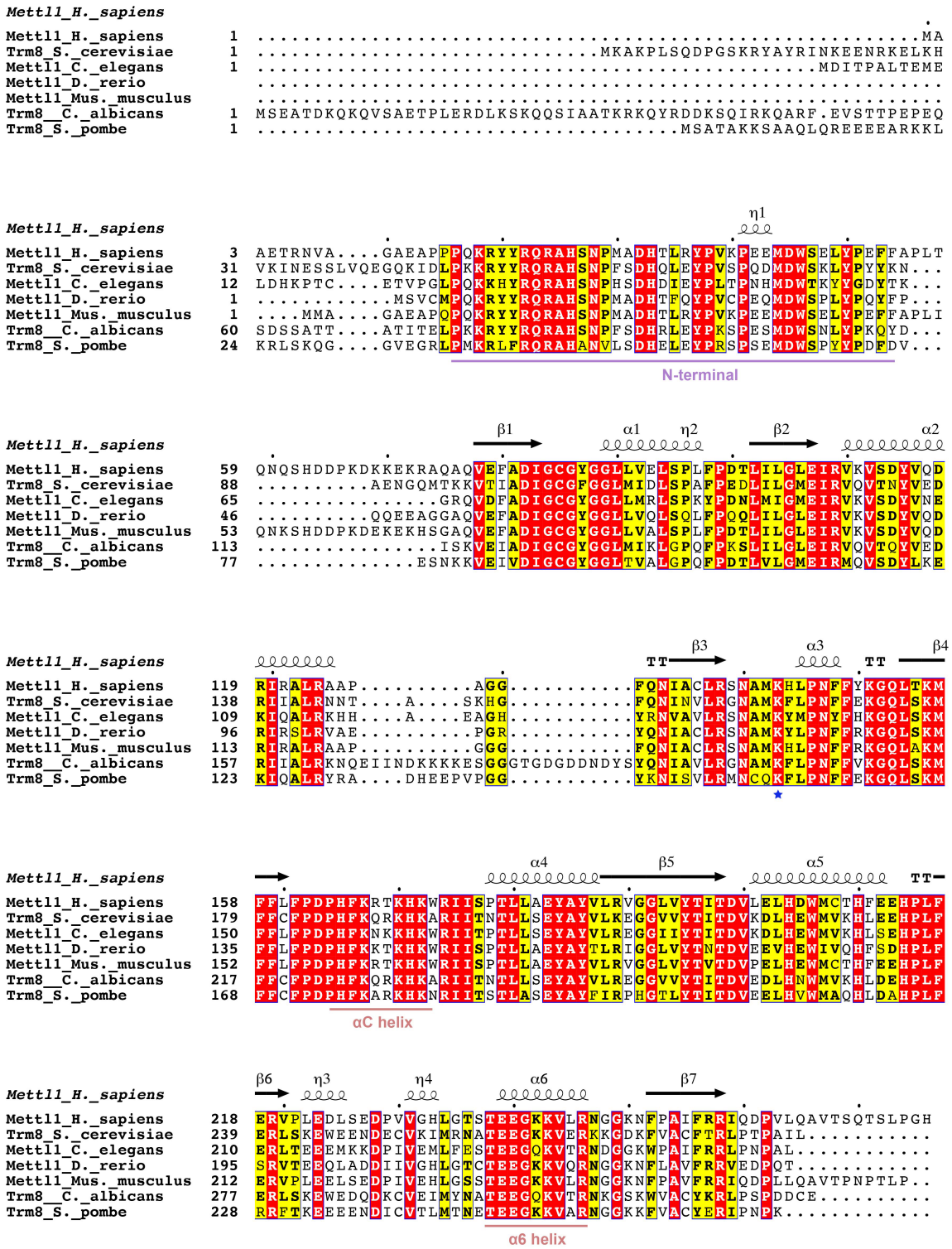


**Extended Data Fig. 4 | Sequence alignment of METTL1 proteins.** The human METTL1 protein sequence was aligned with its respective homologs. The secondary structure diagram for human METTL1 is shown on the top. Conserved residues are shaded in yellow, whereas essentially invariant residues are shown in red. The conserved N-terminal region, aC and a6 helix are underlined. K143 (key residue that interacts with WDR4) is highlighted with a blue star on the bottom. The alignment is performed with the Clustal Omega multiple sequence alignment program (EMBL-EBI) and visualized by ESPript 3.0 server.

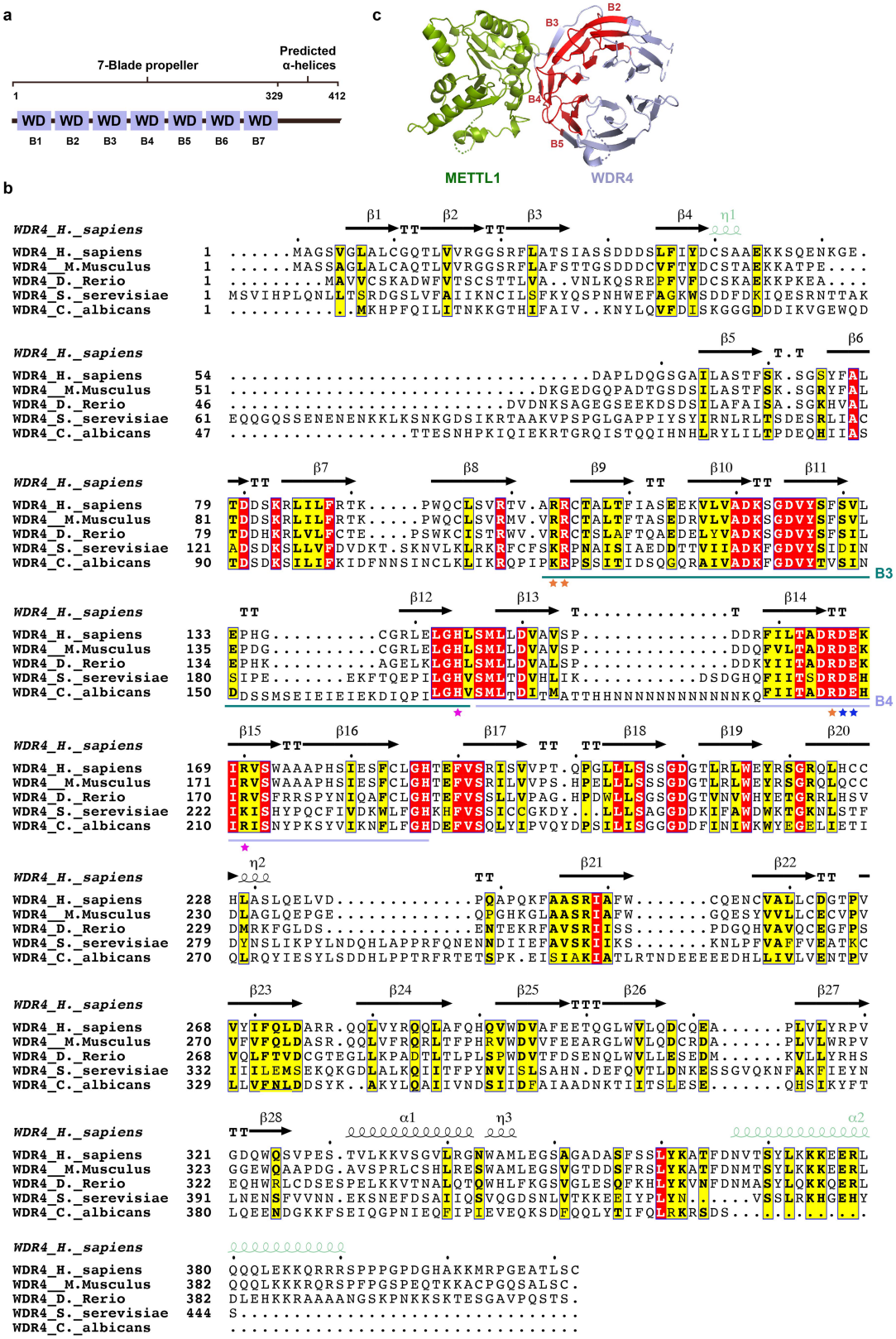


**Extended Data Fig. 5 | Domain organization and sequence alignment of WDR4 proteins.** (**a**) Schematic representation of full-length WDR4 domains based on sequence, secondary structure prediction and experimental structures. WD, WD family repeat domain and are numbered with B1–B7. (**b**) Sequence alignment of WDR4 proteins. The secondary structure diagram (black, based on experimental structure; pale green, based on AlphaFold prediction) for human WDR4 is shown on the top. Conserved residues are shaded in yellow, whereas essentially invariant residues are shown in red. B3 and B4 are underlined in green and blue, respectively. Key residues are highlighted with stars on the bottom. Orange stars, residues involved in tRNA (T-arm) binding; magenta stars, patient related mutagenesis sites; blue stars, METTL1 interaction sites. The alignment is performed with the Clustal Omega multiple sequence alignment program (EMBL-EBI) and visualized by ESPript 3.0 server. (**c**) Structure of METTL1-WDR4-tRNA$^{Phe}$ ternary complex with top view (only METTL1 and WDR4 are shown). The conserved region of B2–B5 (WDR4) is highlighted in red.

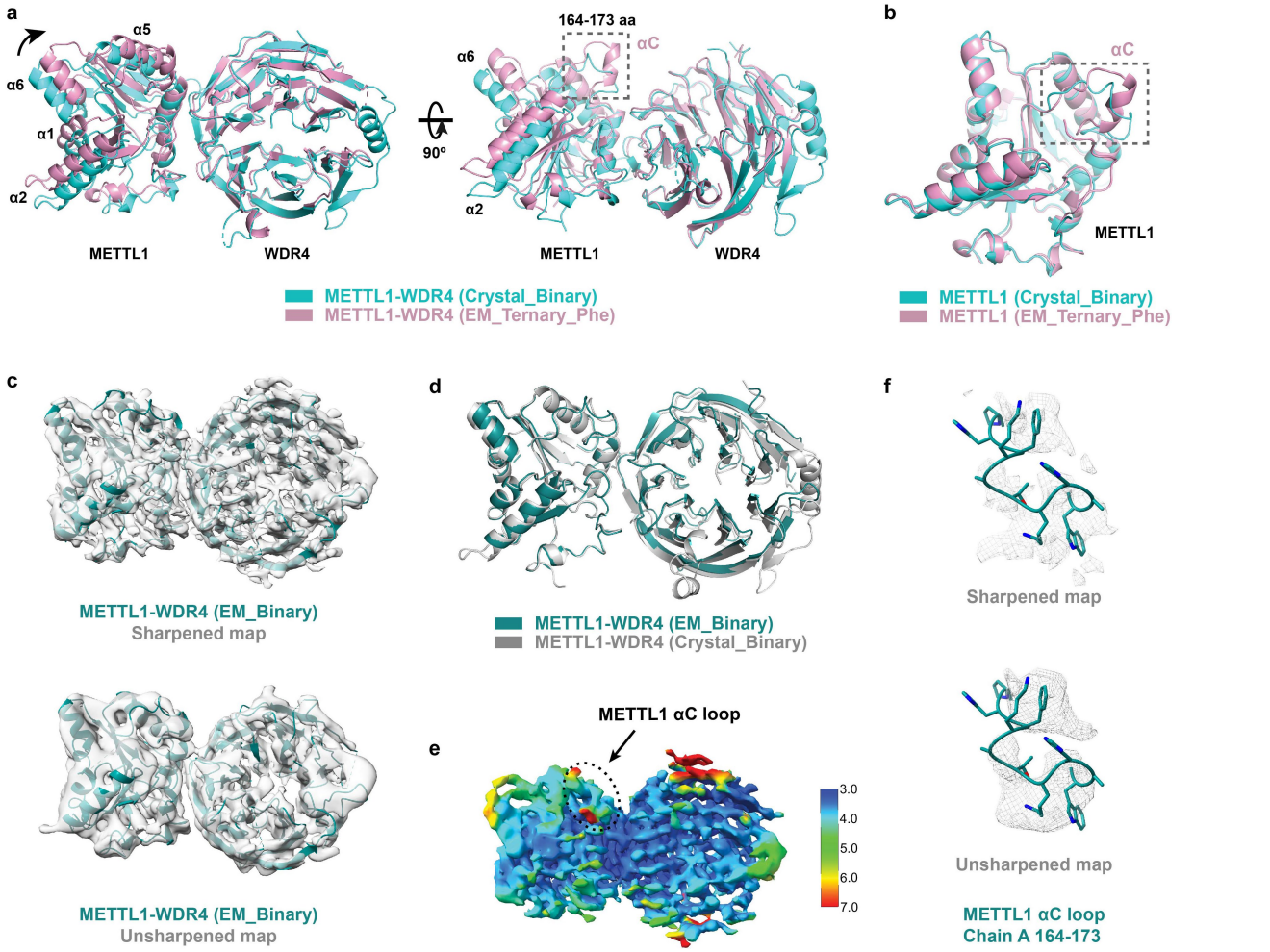


**Extended Data Fig. 6 | The conformational change of METTL1-WDR4 upon tRNA binding.** (**a**)Structure comparison between METTL1-WDR4-tRNA$^{Phe}$ and METTL1-WDR4. The structures are superposed on WDR4 protein. The tRNA in the ternary complex is not shown for a better view. METTL1-WDR4-tRNA$^{Phe}$, pink; METTL1-WDR4, Cyan. The α1, α2, α5 and α6 helices shift toward WDR4 and tRNA side. Structural changes of the residues 164–173 fragment of METTL1 are highlighted with a dash line box. (**b**) Superposition of tRNA-free (cyan) and tRNA bound (pink) states of METTL1. The structures are superposed on METTL1 protein and only only METTL1 are shown. The loop (residues 164–173) connecting α1 and the core fold of METTL1 forms the αC helix upon tRNA binding. (**c**) Binary complex model from METTL1-WDR4-tRNA$^{Phe}$ cryo-EM dataset fit in sharpened (top) and unsharpened (bottom) cryo-EM maps. (**d**) Structure comparison between EM_Binary (teal) and crystal METTL1-WDR4 (gray). The METTL1 protein is superimposed. (**e**) Local resolution of binary complex map. The αC loop of METTL1 region is highlighted with dashed line circle. (**f**)The αC loop of METTL1 (EM_Binary) fit in sharpened (top) and unsharpened (bottom) cryo-EM maps.

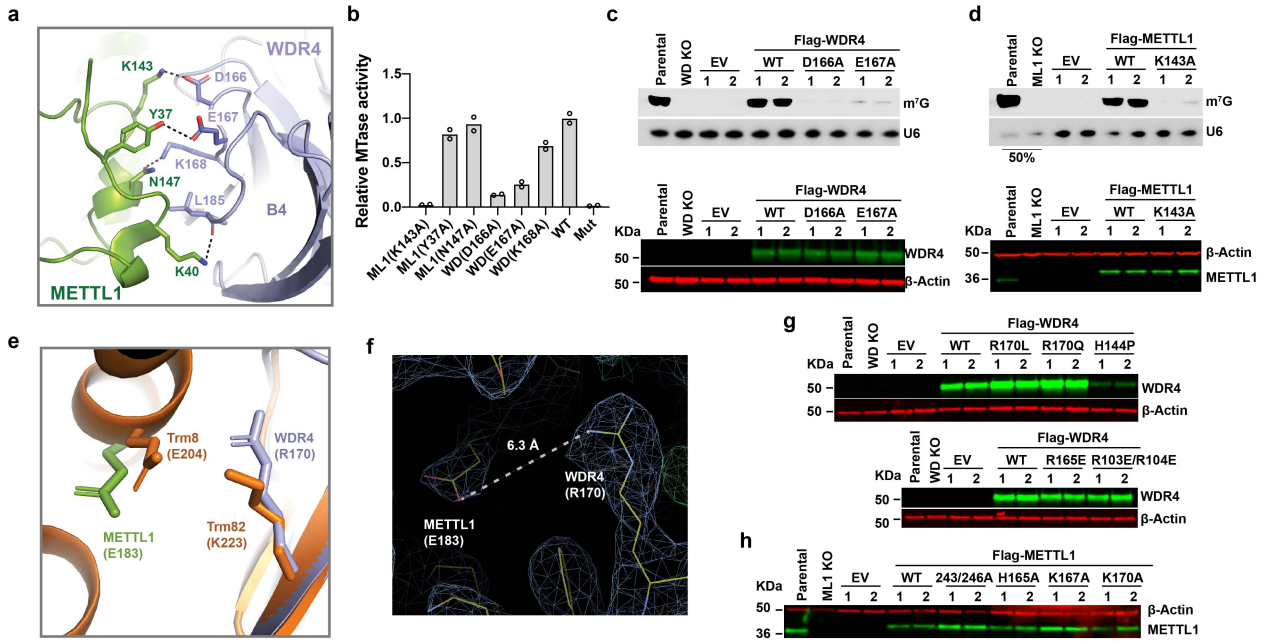


**Extended Data Fig. 7 | Essential residues of METTL1-WDR4 for MTase activity and tRNA recognition.** (**a**) Magnified view of METTL1-WDR4 interface in the crystal binary complex structure. The interactions of key residues are shown in dashed lines. K143 (METTL1) forms a salt bridge with D166 (WDR4); hydrogen bonds are formed between Y37 (METTL1) and E167 (WDR4), N147 (METTL1), and K168 (WDR4), K40 (METTL1) and mainchain of L185 (WDR4). (**b**) Relative methyltransferase activity of METTL1-WDR4 complexes expressed with indicated mutations. WT, wild type; Mut, catalytic dead double mutant (L160A;D163A). Two technical replicates were performed. (**c**–**d**) In vivo rescue experiment with METTL1 or WDR4 carrying indicated mutations in *Wdr4* (KO) cell lines (c) or *Mettl1* (KO) cell lines (d). n = 2, biologically independent samples. Expression of WT and variants METTL1 or WDR4 is checked by western blot (lower panel). For gel source data, see Supplementary Fig. 5-6. (**e**) Structure comparison between METTL1-WDR4 crystal structure (PDB 7U20, METTL1, splitpea; WDR4, light blue) and Trm8-Trm82 (PDB 2VDU, orange). The WDR4 protein is superimposed. (**f**) Distance measurement between METTL1 E183 (OE2) and WDR4 R170 (NH1) in the crystal binary complex structure. 2Fo-Fc map is shown (1.2 σ). Figures were generated in Coot. (**g**, **h**) Western blot detection of overexpressed METTL1 or WDR4 in rescue experiments relative to Fig 2e, j. n = 2, biologically independent samples. For gel source data, see Supplementary Fig. 7.

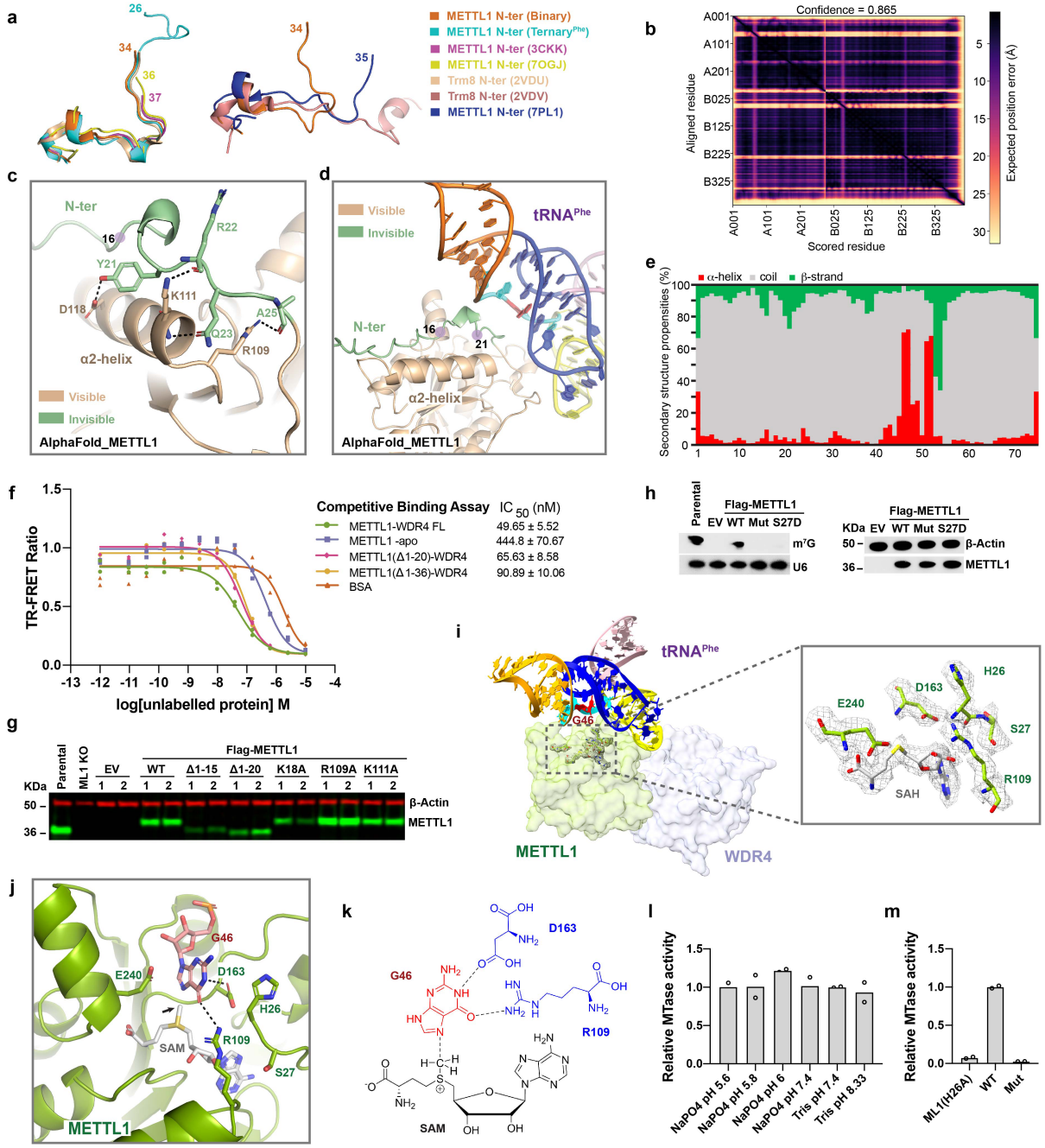


**Extended Data Fig. 8 | The METTL1 N-terminus plays important roles in catalytic regulation.** (**a**) Superimposed METTL1 N-terminus of available structures. The first visible residues of human METTL1 are labeled. (**b**) The IDDT value of the predicted METTL1-WDR4 structure. (**c**) The interactions between the N-terminal and α2 helix in AlphaFold prediction. (**d**) AlphaFold predicted METTL1 is superposed onto METTL1-WDR4-tRNA$^{Phe}$. The predicted residues 16–21 insert into the space between METTL1 and tRNA. (**e**) Residue-specific secondary structure propensities derived from $^{1}H_{N}$, $^{15}N$, $^{13}C'$, $^{13}C\alpha$ and $^{13}C\beta$ chemical shifts assignments. α-helix (red), coil/unstructured (grey), β-strand (green). (**f**) Competitive TR-FRET binding assay of labeled full-length METTL1-WDR4 with unlabeled proteins. The determined $IC_{50}$ is listed. Two technical replicates were performed. (**g**) Western blot detection of overexpressed METTL1 or WDR4 relative to Fig. 3f. n = 2, biologically independent samples. For gel source data, see Supplementary Fig. 7. (**h**) In vivo rescue experiment with indicated mutations in *Mettl1* (KO) cell lines (left). Expression of protein is checked by western blot (right). For gel source data, see Supplementary Fig. 8. (**i**) Key components of the G46 binding cavity fit in sharpened METTL1-WDR4-tRNA$^{Phe}$ cryo-EM map (mesh). Key residues and cofactor SAH are shown in stick. (**j**) Docking model of G46 flipping into the catalytic pocket with SAM bound. The transferred methyl group is indicated by arrow. Relevant elements are adjusted manually to make 180° angle and 2 Å between the guanine-N7 and S-$CH_3$. The potential interactions between METTL1 and the base of G46 are highlighted with dashed lines. (**k**) Schematic diagram of the docking model depicting potential interactions (dashed lines) between G46 and SAM in the METTL1 active site prior to methyl transfer. (**l-m**) Relative methyltransferase activity of METTL1-WDR4 with buffer pH ranging from 5.6 to 8.33 (l) and indicated mutation (m). Two technical replicates were performed.

**Extended Data Table 1 | X-ray and cryo-EM data collection and refinement statistics**

| X-ray data collection and refinement statistics | | Cryo-EM data collection, refinement and validation statistics | | |
|---|---|---|---|---|
| | METTL1-WDR4 (PDB 7U20) | | METTL1-WDR4-tRNA$^{Phe}$-SAH (EMDB-26990) (PDB 8CTH) | METTL1-WDR4-tRNA$^{Val}$ (EMDB-26991) (PDB 8CTI) |
| **Data collection** | | **Data collection and processing** | | |
| Space group | $C222_1$ | Magnification | 81,000 | 81,000 |
| Cell dimensions | | Voltage (kV) | 300 | 300 |
| *a*, *b*, *c* (Å) | 124.41, 194.57, 86.35 | Electron exposure (e–/Å$^2$) | 50.0 | 51.8 |
| α, β, γ (°) | 90.00, 90.00, 90.00 | Defocus range (μm) | -1.0 to -2.0 | 0.8 to -2.2 |
| Resolution (Å) | 47.87-3.09 (3.31-3.09) * | Pixel size (Å) | 1.08 | 0.825 |
| $CC_{1/2}$ | 0.983 (0.320) | Symmetry imposed | C1 | C1 |
| $I / \sigma I$ | 5.1 (0.9) | Initial particle images (no.) | 634,274 | 383,185 |
| Completeness (%) | 99.0 (97.5) | Final particle images (no.) | 266,099 | 115,797 |
| Redundancy | 4.6 (4.7) | Map resolution (Å) | 3.3 | 3.6 |
| | | FSC threshold | 0.143 | 0.143 |
| **Refinement** | | **Refinement** | | |
| Resolution (Å) | 47.87-3.10 | Initial model used (PDB code) | 1EHZ | 3JAG |
| No. reflections | 18971 | Model resolution (Å) | 3.2/3.7 | 3.5/4.1 |
| | | FSC threshold | 0.143/0.5 | 0.143/0.5 |
| $R_{work}$ / $R_{free}$ | 0.2215/0.2708 | Map sharpening *B* factor (Å$^2$) | 125.3 | 147.8 |
| No. atoms | | Model composition | | |
| | | Non-hydrogen atoms | 5,544 | 5,297 |
| | | Protein residues | 495 | 473 |
| | | Nucleotide | 74 | 71 |
| | | Ligands | 1 | 0 |
| Protein | 4327 | R.m.s. deviations | | |
| | | Bond lengths (Å) | 0.003 | 0.011 |
| | | Bond angles (°) | 0.541 | 0.793 |
| Ligand/ion | 15 | Validation | | |
| | | MolProbity score | 1.80 | 1.76 |
| | | Clashscore | 11.80 | 11.62 |
| | | Poor rotamers (%) | 0.00 | 0.49 |
| Water | 12 | Ramachandran plot | | |
| | | Favored (%) | 96.68 | 96.95 |
| | | Allowed (%) | 3.32 | 3.05 |
| | | Disallowed (%) | 0.00 | 0.00 |
| *B*-factors | | | | |
| Protein | 75.04 | | | |
| Ligand/ion | 95.02 | | | |
| Water | 55.40 | | | |
| R.m.s. deviations | | | | |
| Bond lengths (Å) | 0.002 | | | |
| Bond angles (°) | 0.435 | | | |

*Values in parentheses are for highest-resolution shell.

nature portfolio

Corresponding author(s): Richard I. Gregory

Last updated by author(s): Oct 25, 2022

# Reporting Summary

Nature Portfolio wishes to improve the reproducibility of the work that we publish. This form provides structure for consistency and transparency in reporting. For further information on Nature Portfolio policies, see our Editorial Policies and the Editorial Policy Checklist.

## Statistics

For all statistical analyses, confirm that the following items are present in the figure legend, table legend, main text, or Methods section.

| n/a | Confirmed | |
|---|---|---|
| ☐ | ☒ | The exact sample size (*n*) for each experimental group/condition, given as a discrete number and unit of measurement |
| ☐ | ☒ | A statement on whether measurements were taken from distinct samples or whether the same sample was measured repeatedly |
| ☒ | ☐ | The statistical test(s) used AND whether they are one- or two-sided<br>*Only common tests should be described solely by name; describe more complex techniques in the Methods section.* |
| ☒ | ☐ | A description of all covariates tested |
| ☒ | ☐ | A description of any assumptions or corrections, such as tests of normality and adjustment for multiple comparisons |
| ☐ | ☒ | A full description of the statistical parameters including central tendency (e.g. means) or other basic estimates (e.g. regression coefficient) AND variation (e.g. standard deviation) or associated estimates of uncertainty (e.g. confidence intervals) |
| ☒ | ☐ | For null hypothesis testing, the test statistic (e.g. *F*, *t*, *r*) with confidence intervals, effect sizes, degrees of freedom and *P* value noted<br>*Give P values as exact values whenever suitable.* |
| ☒ | ☐ | For Bayesian analysis, information on the choice of priors and Markov chain Monte Carlo settings |
| ☒ | ☐ | For hierarchical and complex designs, identification of the appropriate level for tests and full reporting of outcomes |
| ☒ | ☐ | Estimates of effect sizes (e.g. Cohen's *d*, Pearson's *r*), indicating how they were calculated |

*Our web collection on statistics for biologists contains articles on many of the points above.*

## Software and code

Policy information about availability of computer code

| | |
|---|---|
| Data collection | X-ray diffraction data were indexed and integrated using RAPS pipeline from APS Chicago; Cryo-EM data were collected using SerialEM (version 3.8.5) or Latitude-S (Gatan Microscopy Suites software package, MODEL 700.LS.731). Northwestern blot and Western blot data were imaged using the ECL method or the Odyssey Imaging System, Image Studio (Li-Cor, Version 5.2.5), respectively. TR-FRET signals were acquired on a PHERAstar microplate reader (BMG Labtech Model FS). Scintillation signals were measured using the Tri-Carb instrument (Perkin Elmer Model 2910 TR). NMR data was acquired using Topspin (Bruker, version 3.4). |
| Data analysis | Cryo-EM data analysis: MotionCor2 (version 1.4.0), Relion (version 3.1.3), cryoSPARC (version 3.3.1). Model building and refinement for cryoEM structure: Coot (version 0.8.9.2), PHENIX (version 1.20.1-4487-000), AlphaFold (version 2.2), Rosetta(version 3.12). Model building and refinement for crystal structure: Coot (version 0.8.9.2), PHENIX (version 1.20.1-4487-000), autoBUSTER (version 2.10.4) and MOLPROBITY (version 4.2). NMR data was processed with NmrPipe (version 01/29/2021) and analyzed with CCPNmr (version 2.4). Sequence alignment: Clustal Omega (accessed through the EMBL-EBI server) and ESPript (version 3.0). Data plotting: GraphPad Prism (version 8). Molecular Graphics: ChimeraX (version 1.2.5), PyMOL (version 2.1). |

For manuscripts utilizing custom algorithms or software that are central to the research but not yet described in published literature, software must be made available to editors and reviewers. We strongly encourage code deposition in a community repository (e.g. GitHub). See the Nature Portfolio guidelines for submitting code & software for further information.

## Data

Policy information about availability of data

All manuscripts must include a data availability statement. This statement should provide the following information, where applicable:

- Accession codes, unique identifiers, or web links for publicly available datasets
- A description of any restrictions on data availability
- For clinical datasets or third party data, please ensure that the statement adheres to our policy

The CryoEM structures of METTL1-WDR4-tRNA (Phe) and METTL1-WDR4-tRNA (Val), and X-ray crystal structure of METTL1-WDR4 have been deposited to the Protein Data Bank (PDB) under accession number 8CTH, 8CTI and 7U20, respectively. The cryo-EM density maps of METTL1-WDR4-tRNA (Phe) and METTL1-WDR4-tRNA (Val) have been deposited in the Electron Microscopy Data Bank (EMDB) under accession numbers 26990 and 26991. Several structural coordinates in the PDB database were used in this study, which can be located by accession numbers 1EHZ, 2VDU, 3JAG, 3CKK, 7OGJ, 2VDV and 7PL1. NMR resonance assignments were deposited to the BMRB under accession number 51362.

## Human research participants

Policy information about studies involving human research participants and Sex and Gender in Research.

| | |
|---|---|
| Reporting on sex and gender | N/A |
| Population characteristics | N/A |
| Recruitment | N/A |
| Ethics oversight | N/A |

Note that full information on the approval of the study protocol must also be provided in the manuscript.

# Field-specific reporting

Please select the one below that is the best fit for your research. If you are not sure, read the appropriate sections before making your selection.

☒ Life sciences ☐ Behavioural & social sciences ☐ Ecological, evolutionary & environmental sciences

For a reference copy of the document with all sections, see nature.com/documents/nr-reporting-summary-flat.pdf

# Life sciences study design

All studies must disclose on these points even when the disclosure is negative.

| | |
|---|---|
| Sample size | Sample sizes were not predetermined. Cryo-EM images were collected until structures of satisfactory quality were solved, which suggested sufficient sample size. |
| Data exclusions | In cryo-EM data processing, the "junk" particles were excluded that could not be classified into useful 3D reconstructions. This is a widely used and accepted practice in the cryo-EM field. No other data were excluded from analysis. |
| Replication | All experiments were performed independently at least two times with similar results, as described in the figure legends. |
| Randomization | Proteins and cells were randomly allocated to the wells or tubes in each experimental group. |
| Blinding | No blinding was used in this study because subjective analysis was not needed. Each experiment was performed using consistent methods. |

# Reporting for specific materials, systems and methods

We require information from authors about some types of materials, experimental systems and methods used in many studies. Here, indicate whether each material, system or method listed is relevant to your study. If you are not sure if a list item applies to your research, read the appropriate section before selecting a response.

## Materials & experimental systems

| n/a | Involved in the study |
|---|---|
| ☐ | ☒ Antibodies |
| ☐ | ☒ Eukaryotic cell lines |
| ☒ | ☐ Palaeontology and archaeology |
| ☒ | ☐ Animals and other organisms |
| ☒ | ☐ Clinical data |
| ☒ | ☐ Dual use research of concern |

## Methods

| n/a | Involved in the study |
|---|---|
| ☒ | ☐ ChIP-seq |
| ☒ | ☐ Flow cytometry |
| ☒ | ☐ MRI-based neuroimaging |

# Antibodies

Antibodies used

Anti-7-methylguanosine (m7G) (Clone 4141-13, Monoclonal antibody, Host Mouse, Isotype IgG2aκ, MBL International, Cat# RN017M; RRID: AB_2725740, 1: 1000)
Anti-β-Actin (Polyclonal antibody, Host Goat, Isotype IgG, Abcam, Cat# Ab8229; RRID: AB_306374, 1:10000)
Anti-METTL1 (Polyclonal antibody, Host Rabbit, Isotype IgG, Proteintech, Cat# 14994-1-AP, 1: 2000)
Anti-WDR4 (Clone EPR11052, Monoclonal antibody, Host Rabbit, Isotype IgG, Abcam,Cat# ab169526, 1: 2000)

Validation

All antibodies used in this study are commercially available and have been validated by the manufacturers' and/or previous publications.
Anti-7-methylguanosine (m7G): https://www.mblintl.com/products/rn017m/
Anti-β-Actin: https://www.abcam.com/beta-actin-antibody-loading-control-ab8229.html
Anti-METTL1: https://www.ptglab.com/products/METTL1-Antibody-14994-1-AP.htm
Anti-WDR4: https://www.abcam.com/wdr4-antibody-epr11052-ab169526.html

# Eukaryotic cell lines

Policy information about cell lines and Sex and Gender in Research

Cell line source(s)

Mouse R1/E ESCs is gift from Dr. Lizi Wu's lab (University of Florida) (ATCC, SCRC-1036).Mouse METTL1 KO R1/E ESCs were generated in our previous study (Lin, Shuibin, et al. Molecular cell, 2018). WDR4 KO were generated from mouse R1/E ESCs (ATCC, SCRC-1036) following our previous protocol (Lin, Shuibin, et al. Molecular cell, 2018).

Authentication

METTL1 KO R1/E ESCs and WDR4 KO R1/E ESCs were obtained by CRISPR and verified by immunoblotting or PCR genotyping as previous described. All cells were frequently checked by their morphological features and functions. No other authentication was performed.

Mycoplasma contamination

All cell lines were tested to be mycoplasma-negative by Mycoplasma Detection kit.

Commonly misidentified lines
(See ICLAC register)

No commonly misidentified cell lines were used in this study.